# Assessing impact of real-world aging on Cu-redox half cycles of a Cu-SSZ-13 SCR catalyst via transient response measurements and kinetic modeling☆

Dhruba J. Deka [a], Rohil Daya [b], Austin Ladshaw [a], Dylan Trandal [b], Saurabh Y. Joshi [b], William P. Partridge [a],*

[a] Oak Ridge National Laboratory, 2360 Cherahala Blvd., Knoxville, TN 37932, United States
[b] Cummins Inc, 1900 McKinley Ave, Columbus, IN 47201, United States

## ARTICLE INFO

## ABSTRACT

The SCR reaction on Cu-SSZ-13 is a redox process consisting of a reduction half-cycle (RHC) and an oxidation half-cycle (OHC). Despite extensive efforts to understand hydrothermal aging and sulfur poisoning, the impact of real-world aging on the SCR activity of Cu-SSZ-13 has not been reported. This work employs a transient response methodology consisting of experiments and kinetic models to investigate the SCR redox cycles at intra-catalyst locations of commercial Cu-SSZ-13 monolith catalysts in their degreened and real-world aged states, in the temperature range of 200–450 °C. Moreover, $H_2$-TPR, $NH_3$-TPD, $SO_2$-TPD, ICP-OES and solid-state NMR were performed to investigate the catalyst properties. Sulfur aging and dealumination caused by real-world exposure decreased the reducible Cu density and SCR performance. Real-world aging was found to selectively slow OHC more than RHC, mainly due to lower mobility of the Cu ions coordinated to sulfur-related species leading to decreased formation of Cu-dimers necessary for OHC.

## 1. Introduction

The commercially available Cu-SSZ-13 catalyst is applicable for abatement of $NO_x$ emissions from lean-burn engine vehicles [1]. Despite the presence of excess $O_2$ in the lean-combustion exhaust, these Cu-exchanged small-pore zeolites can selectively reduce $NO_x$ to $N_2$ using $NH_3$ as the reductant, a reaction commonly known as selective catalytic reduction (SCR) of $NO_x$. In the past decade, Cu-SSZ-13 has been instrumental in meeting on-road-vehicle and non-road emission regulations and thereby enhancing environmental and public health.

The Cu-SSZ-13 catalyst can achieve complete $NO_x$ conversion at temperatures as low as 200 °C and maintain high activity at higher temperatures (as high as 550 °C) if sufficient $NH_3$ is available for reaction [2,3]. Isolated Cu sites have been shown to be the SCR active sites [4–9], and there are two different types of these isolated Cu sites present in Cu-SSZ-13: $Z_2Cu$ sites coordinated with two paired framework Al in the 6-membered-ring windows (6MR) and $Z_1CuOH$ sites coordinated with single framework Al in the 8MR cages [7]. Both of these isolated Cu ions act as Lewis-acid as well as redox sites and show similar activity for SCR reaction. The SCR reaction is a redox reaction during which Cu sites are cycled between Cu(I) and Cu(II) by the reduction half cycle (RHC) and the oxidation half cycle (OHC) [4,6,9]. Bronsted-acid sites (ZH) are also present in these materials that can store additional $NH_3$, which can be used for $NO_x$ reduction if $NH_3$ is temporarily depleted from the gas stream.

Commercial feasibility of any catalytic system requires not only high activity and selectivity, but also excellent long-term durability under operating conditions. The hydrothermal stability of Cu-SSZ-13 has been investigated thoroughly by various studies, which show that NO reduction activity is maintained by the catalyst after hydrothermal aging (HTA) up to 900 °C [3,10,11]. Luo et al. reported that HTA can transform $Z_1CuOH$ sites to $Z_2Cu$, while consuming Bronsted-acid sites [12,

* Corresponding author.
  *E-mail address:* partridgewp@ornl.gov (W.P. Partridge).

13]. Despite SSZ-13 zeolite's good thermal durability for engine-exhaust applications, dealumination of the zeolite framework may occur at high temperatures possible in engine applications. Xi et al. observed minor SSZ-13 dealumination after HTA at 650 °C for 100 h [14], and the onset of zeolite-framework collapse above 800 °C.

Real-world or field applications may expose the SCR catalyst to various fuel and lubricant related impurities and chemical poisons originating from upstream aftertreatment components, which leads to aging pathways in addition to HTA. For systems under normal operation conditions, deposits from platinum group metals (PGM) volatilized from upstream catalysts (e.g., diesel oxidation catalyst, DOC) occurs in very small concentrations (ppm levels) that do not result in significant aging with percent-level active Cu. However, lubricant-originating phosphorus may exist at higher concentrations, and fuel-born sulfur (S) that oxidizes to $SO_2$ or $SO_3$ during combustion or over the DOC/DPF may permeate the entire catalyst length and lead to S-related aging pathways. Degraded SCR performance of Cu-SSZ-13 due to sulfur poisoning has been reported [14–17]. Jangjou et al. reported that in the presence of $NH_3$, $SO_2$ can deactivate both $Z_2Cu$ and $Z_1CuOH$ sites, albeit with different poisoning routes [15]; $SO_2$ poisons $Z_2Cu$ via formation of ammonium sulfate that blocks the $Z_2Cu$ sites, while it poisons $Z_1CuOH$ via formation of copper bisulfite. Desulfation of ammonium sulfates occurs at lower temperatures than required for copper bisulfites. In the presence of $O_2$, these bisulfites can further convert to more stable bisulfates and sulfates, thereby necessitating even higher desulfation temperatures. The $Z_2Cu$ sites were not affected by sulfur exposure in the absence of $NH_3$. Xi et al. arrived at similar conclusions that $Z_2Cu$ sites are less susceptible to sulfur poisoning and can be more readily desulfated than $Z_1CuOH$ sites [14]. Since HTA converts $Z_1CuOH$ to $Z_2Cu$, they proposed HTA as an effective preventive measure for avoiding sulfur poisoning.

The aforementioned HTA and sulfur poisoning studies followed laboratory-based treatment of the catalyst under controlled aging conditions. During field aging under real-world on-road driving conditions, the catalysts are exposed to a multitude of temperature and sulfur-exposure conditions, and the resulting aging is not fully captured by laboratory aging methods. Despite and due to the complexity of field aging, the literature is sparce regarding its impact on Cu-SSZ-13 SCR catalysts. To our knowledge, there is only one publication involving field aged Cu-SSZ-13 in the literature, but it does not investigate the detail of Cu-redox half-cycle kinetics and deactivation mechanisms; Xi et al. reported the SCR activity of a field returned sample before and after desulfation in the lab [14]. More detailed studies addressing the SCR redox half cycles are required to better understand the impact of field aging on the catalyst performance. The current useful life requirement for SCR catalysts in heavy heavy-duty (HHD, or Class 8) applications, is 435,000 miles as per U.S. Environmental Protection Agency (EPA) and California Air Resources Board (CARB) [18]. This requirement is increased by CARB to 600,000 miles by the year 2027, and 800,000 miles by 2031 in their proposed Heavy-Duty Engine and Vehicle Omnibus Regulation [18]. Thus, understanding real-world field aging is timely and of utmost importance, so that more durable catalyst technologies can be developed to meet these stringent and challenging regulations.

In a separate publication we have described a transient-response methodology composed of a transient-response Cu-redox (TRCR) protocol and related catalyst half-cycle modeling, and its application for experimentally investigating performance of a degreened (DG) commercial Cu-SSZ-13 SCR catalyst from a Cu-redox half-cycle perspective and quantifying the global half-cycle kinetic parameters [19]. Here, we report application of that methodology along with conventional characterization to investigate field aging of the same commercial Cu-SSZ-13 SCR catalyst and compare the measured aging impacts to the degreened state. The TRCR protocol was used to experimentally evaluate the impact of field aging on relative RHC and OHC rates, reducible Cu, and steady state (SS) SCR Cu(II)-Cu(I) partitioning. The RHC and OHC

kinetic models were used with the TRCR-protocol data to determine half-cycle kinetic parameters and quantitatively assess the impact of field aging. A combination of characterization techniques including $H_2$ temperature-programmed reduction (TPR), sulfur-species temperature-programmed desorption (TPD), $NH_3$ TPD, inductively coupled plasma optical-emission spectrometry (ICP-OES) and solid-state nuclear-magnetic-resonance (NMR) spectroscopy ($^{27}Al$ and $^{29}Si$) were used to understand how field aging influences the Cu-SSZ-13 material properties. The ICP-OES results revealed sulfur in the real-world field-aged (FA) catalyst, and the distribution of various sulfated species were identified via sulfur-species TPD. The NMR results indicated dealumination of the FA-sample framework aluminum. Both sulfur aging and dealumination degrade active-Cu site density. Consequently, field aging was found to degrade the low-temperature SCR activity of Cu-SSZ-13, but with differing impact on RHC and OHC. Even though field aging results in loss of active Cu sites, the SCR turnover frequency is also impacted which suggests that active site loss is not the only reason behind SCR performance degradation and that the half cycle kinetics are also affected. Application of the transient response methodology indeed quantified the half-cycle-specific kinetic impacts of field aging. To our knowledge, this is the first publication to report field impacts on the SCR Cu-redox cycle and quantify related impacts on RHC and OHC global kinetic parameters.

## 2. Experimental details

### 2.1. Catalyst samples

The commercial Cu-SSZ-13 catalyst washcoated on cordierite monolith (300 cpsi) used in this study was provided by Cummins Inc. The catalyst had a Cu loading of approximately 2.4%, and an Si/Al ratio of 15. Both the DG and FA catalyst studies used 1-inch-long monolith cores. Prior to DG SCR activity evaluation, the catalyst was degreened at 550 °C for 4 h under 10% $O_2$, 7% $H_2O$ and 8% $CO_2$ in Argon balance (space velocity = 40000/h). The FA Cu-SSZ-13 core was exposed to unmonitored on-road HHD diesel-vehicle for 538,000 miles (greater than the regulation 435,000-miles end of useful life), and was selected as its $NH_3$-capacity loss was representative of the 90th percentile from a population analysis of tens of thousands of systems across different platforms. The FA sample used here was taken from the front 2–3inch region of a larger FA sample.

### 2.2. Catalyst characterization

#### 2.2.1. $H_2$ temperature-programmed reduction (TPR)
The $H_2$-TPR measurements were performed using a Micromeritrics AutoChem II 2090 equipped with TCD detector and using a 250-mg sample of crushed catalyst core (washcoat + monolith). Samples were pre-treated at 550 °C for one hour under ultra-high purity air and then cooled to 50 °C. An argon purge flow was used to flush air from the sample before introducing a 30-sscm flow of 5% $H_2$ in Ar. The sample was heated from 50 °C to 550 °C at a ramp rate of 10 °C/min to implement $H_2$-TPR. The TCD was used to monitor the overall TPR profile, and a downstream quadrupole mass spectrometer (Pfeiffer OmniStar) was used to monitor specific gas concentrations in the exit stream.

#### 2.2.2. Sulfur species temperature-programmed desorption (TPD)
Sulfur loading of the FA catalyst was investigated via TPD of sulfated species from 250 mg of crushed-monolith sample with no pretreatment (as received), and heating from room temperature to 1000 °C at a 10-°C/min ramp rate under a 30-sscm Ar flow (Airgas, 0.001% purity). The same Micromeritrics AutoChem II 2090 mentioned above was used for these experiments. Desorbed $SO_2$ was monitored via the 64-$m/z$ signal from a quadrupole mass spectrometer (Pfeiffer OmniStar).

### 2.2.3. Elemental analysis

The elemental composition (Cu, Si, Mg, S, P) of the DG and FA Cu-SSZ-13 catalysts was determined by inductively coupled plasma optical emission spectroscopy (ICP-OES) and inductively coupled plasma mass spectroscopy (ICP-MS) at Galbraith Laboratories Inc (Knoxville, TN).

### 2.2.4. Solid state nuclear magnetic resonance (NMR)

Samples for the NMR experiments were prepared by carefully scraping catalyst washcoat from the cordierite-monolith substrate, and sieving to remove any broken cordierite particles/flakes. The Fourier transform solid-state NMR spectra of $^{27}$Al and $^{29}$Si were collected on a Bruker NEO 400 MHz instrument equipped with a Doty Scientific DSI-1630 broadband probe operating at room temperature at Triclinic Labs (Lafayette, IN). The samples were packed into 4-mm diameter $Si_3N_4$ rotors with GF Torlon® caps and spun at 12 kHz. The $^{27}$Al NMR spectra were acquired with Larmor frequency of 104.27 MHz under a Block decay pulse sequence utilizing the following data acquisition conditions: 90° pulse width of 5.00 μs, 68.5-kHz spectral width, 15-ms acquisition time with 1-s relaxation delay time. Similarly, the $^{29}$Si NMR spectra were acquired with Larmor frequency of 79.50 MHz under a Block decay pulse sequence utilizing the following data acquisition conditions: 90° pulse width of 5 μs, 39.7-kHz spectral width, 51.6-ms of acquisition time with 1-s relaxation delay time.

### 2.2.5. NH₃ temperature-programmed desorption (TPD)

Ammonia adsorption capacity and coordination on the DG and FA catalyst cores was determined via NH$_3$ TPD using a base flow of 5% H$_2$O in Ar at 40000/h space velocity in a catalyst core reactor setup described below. The catalyst samples were pretreated with 200 ppm NO + 5% O$_2$ flow at 400 °C to clean the surface by removing any adsorbed NH$_3$, cooled to 200 °C under 5% O$_2$ flow, and maintained at 200 °C under 5% O$_2$ for an hour to ensure complete oxidation of the Cu sites. The pre-oxidized sample was saturated with NH$_3$ via a 200-ppm NH$_3$ (balance Ar) flow at 200 °C for 1 h. The reactor was then flushed using the base flow at 200 °C for 1.5 h to flush gas-phase NH$_3$ and remove weakly bound NH$_3$. The NH$_3$ TPD was implemented by ramping the temperature from 200 °C to 540 °C at a 10-°C/min rate. Desorbed NH$_3$ was monitored by an FTIR (MKS Instruments Multigas 2030HS). All of the experimental steps (pre-treatment, NH$_3$ adsorption, flushing and TPD) included the 5% H$_2$O base flow.

### 2.3. Catalyst core reactor setup

The catalyst-core reactor provides for dynamic control of the temperature and flow composition exposed to the catalyst sample [19]. A half-inch ID quartz tube nested in a tube furnace housed the 1-inch long and 21-cell (300 cpsi, 5 ×5 with corner cells missing) monolith catalyst sample. The reactor includes four valves (Valco, 4-way switching valves) to switch between four parallel Span (resulting in 200-ppm NO, 200-ppm NH$_3$, 5% O$_2$, and 5% H$_2$O in the reactor feed) and Blank (Ar) flows, and feed any combination of these gas streams to the catalyst sample; for the experiments reported here 5% H$_2$O was used throughout, and only the NO, NH$_3$ and O$_2$ flows were switched. Gas standards (0.001% purity level, Air Gas) were used for NO, NH$_3$ and O$_2$ control, and a 52 °C H$_2$O bubbler was used for the H$_2$O control. Argon balance gas was supplied from a cryogenic liquid argon dewar. The four parallel Span/Blank flows were added to a parallel Ar-balance flow to achieve a space velocity of 40000/h. An FTIR (MKS Instruments Multigas 2030HS) analyzed the reactor effluent for integral-performance measurements.

A spatially resolved capillary inlet mass spectrometer (SpaciMS) was used to perform intra-catalyst measurement of reactive gas species. This technique was previously employed in various emissions-control catalyst studies, such as three-way catalysts (TWC), lean NO$_x$ trap (LNT), diesel oxidation catalysts (DOC), and particulate filter catalysts to understand the spatiotemporal evolution of reactive species and network

and sequences of reactions along the catalyst flow channel [20–22]. The SpaciMS setup consisted of two hollow quartz capillaries (75-μm ID, 150-μm OD, Polymicro), one fixed at catalyst inlet and the other positioned inside the central catalyst flow channel. The intra-catalyst capillary position could be translated to sample various locations along the catalyst length with a spatial resolution less than 1/16 L (1 L: full catalyst length, 0 L: catalyst inlet). The capillaries sample ~10 μL/min (0.02% of the channel flow), occupy 1.8% of the probed-channel open area, and are oriented to reset in the channel corner; this configuration has been shown to be practically noninvasive [22–24]. A multi-port valve (Valco, 12-port, SC type) was used to select between the catalyst-inlet and intra-catalyst capillaries for analysis, and the entire capillary sampling system was maintained at > 200 °C to avoid intra-capillary condensation and deposit formation. A quadrupole mass spectrometer (Pfeiffer, PrismaPlus QME 220) was used to analyze the capillary sample flows.

### 2.4. Transient-response Cu-redox cycle protocol

A transient-response Cu-redox (TRCR) protocol as shown in Fig. 1(a) was used to evaluate the SCR redox half-cycle kinetics of the DG and FA catalysts, following a broader transient-response methodology described in a separate publication [19]. The protocol includes three SCR steps (SCR-a, SCR-b, SCR-c), three RHC steps (RHC-a, RHC-b and RHC-c), and three OHC steps (OHC-a, OHC-b, OHC-c), with the various like steps being initiated in different ways. In general, the flow arrangements were NO+NH$_3$ +O$_2$ for SCR, NO+NH$_3$ for RHC and NO+O$_2$ for OHC (NO: 200 ppm, NH$_3$: 200 ppm, O$_2$: 5%), with a continuous 5% H$_2$O in Ar balance flow throughout the experiment.

The N$_2$ formation during these steps was measured using SpaciMS at five different intra-catalyst locations: 1/8 L, 1/4 L, 3/8 L, 1/2 L and 3/4 L (where 0 L: catalyst inlet, and 1 L: catalyst exit). A typical intra-catalyst N$_2$ formation transient is shown in Fig. 1(b). One interesting feature in these N$_2$ transients is the "conversion inflection" observed at SCR onset and characterized by a sharp rise in N$_2$ concentration (see SCR-b and SCR-c onsets) and subsequent slow drop to the SS-SCR N$_2$ level. Such transient increase in N$_2$ formation at SCR onset above and prior to the SS-SCR level is called a conversion inflection (CI), and Partridge et al. associated these with transient imbalances between the RHC and OHC rates in their combined experimental and kinetic modeling work [21]. For example, at SCR-b onset, the entire Cu inventory is in the reduced Cu(I) state; therefore, OHC is the only half-cycle reaction that can occur at SCR-b onset and is fully responsible for the step-like N$_2$ formation. As OHC progresses beyond SCR-b onset, the Cu(II) concentration increases leading to RHC activity onset and a corresponding increase in the RHC rate. In the early-SCR-b times within the CI tail beyond the CI peak, dynamic Cu(II)-Cu(I) partitioning along with NO and NH$_3$ conversion cause the RHC rate to increase as the OHC rate decreases, until a point when both half-cycle rates balance at SS SCR; the CI-tail shape is indicative of this dynamic rate balancing and the RHC and OHC kinetics [21]. Since the entire Cu inventory is in the Cu(II) state prior to SCR-c onset, an entirely opposite sequence of dynamic RHC and OHC rate balancing is observed, where SCR-c onset starts with pure RHC. The shape and intensity of these CIs provide valuable information about the RHC and OHC kinetics. For example, if OHC kinetics are faster than RHC, the SCR-b CI will be higher than the SCR-c CI, and vice versa. In Section 3.7, this concept is used to understand how the RHC and OHC kinetics are uniquely impacted by field aging.

The RHC steps are used to count Cu(II) sites, and in the process each reduced Cu site forms one equivalent N$_2$ molecule [25–27]. Therefore, the area under the RHC-a N$_2$ transient provides a measure of the total reducible-Cu density. The RHC-b step involves reducing all the Cu(II) ions present at SS SCR (SCR-a step), and hence, the area under the RHC-b N$_2$ transient is a measure of the Cu(II) amount at SS SCR. Therefore, the ratio of the RHC-b to RHC-a areas indicates the Cu(II) fraction and
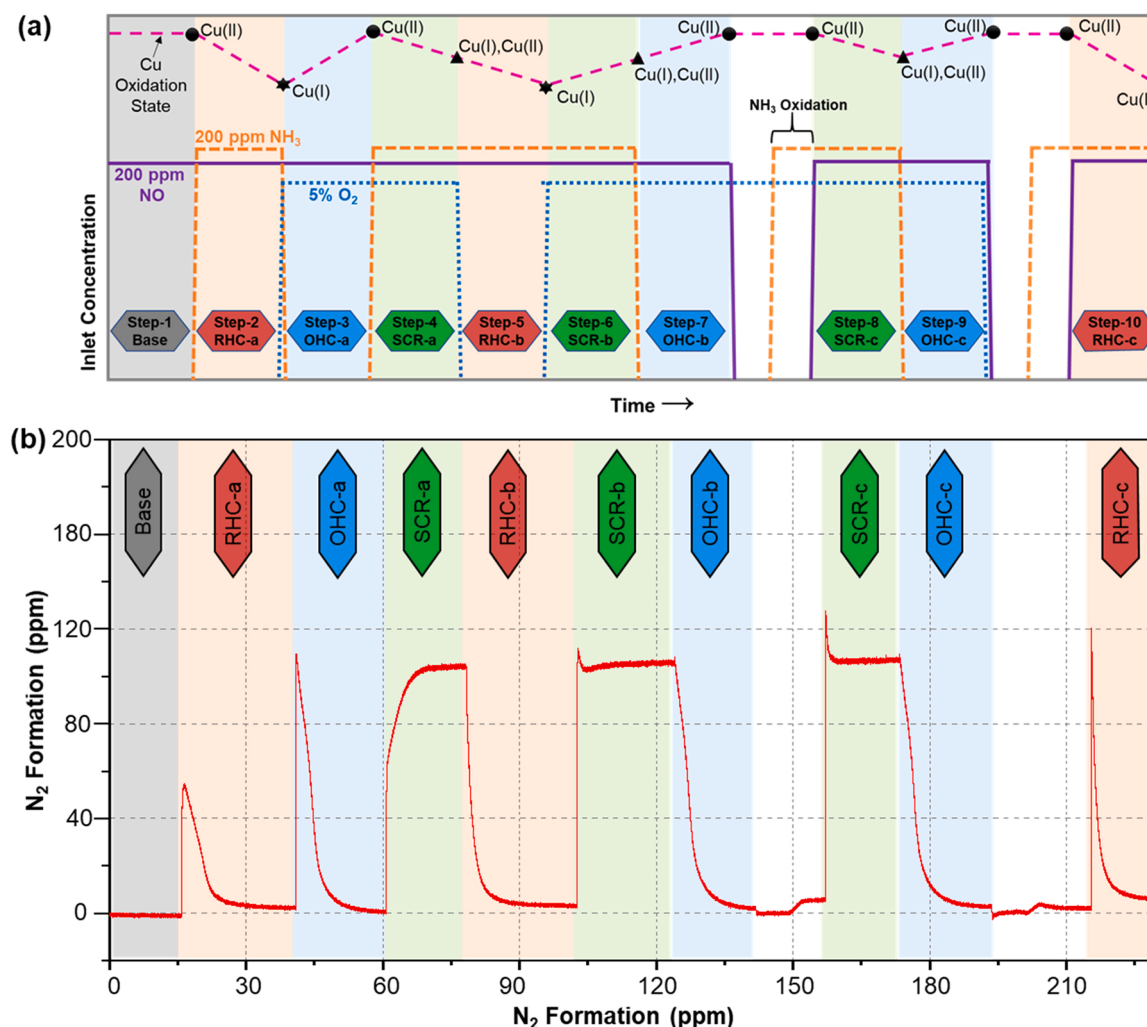
**Fig. 1.** (a) Different steps of the TRCR protocol, corresponding gas flow combinations, and representative Cu oxidation state at each step. (b) Representative $N_2$ formation transient measured through the TRCR protocol.

correspondingly the Cu(II)-Cu(I) partitioning at SS SCR. The TRCR protocol thus allows in-operando measurement of Cu oxidation state speciation using a generally common laboratory setup, and provides similar and complementary information for better understanding of active sites to that associated more expensive and less-accessible facilities such as X-ray absorption spectroscopy [6]. This ability to quantify reducible Cu density and Cu(II) fraction at SS SCR is used in the Results and Discussion Section to determine how the relative RHC and OHC rates evolve as a function of temperature, catalyst location, and field aging.

In addition to their use for counting Cu, the RHC and OHC $N_2$ transients are useful in formulating SCR-redox kinetic models. These models with the TRCR protocol form a transient-response methodology for quantifying the RHC and OHC kinetic parameters, and investigating how they are selectively impacted by field aging [19]. In Sections 3.8 and 3.9, RHC and OHC kinetic models are described and applied to fit the transient TRCR-protocol data and compare the kinetic parameters of the DG and FA catalysts.

## 3. Results and discussion

Field aging affects the physical and chemical properties of the Cu-SSZ-13 catalyst as well as its SCR performance. In Sections 3.1–3.5, we present characterization results to assess material-property changes including Cu speciation, reducible-Cu density, Bronsted-acid site concentration, dealumination, and impurity contamination. Section 3.6 and thereafter focuses on the SCR performance of the DG and FA catalysts, and how field aging affects the SCR redox half cycles.

### 3.1. $H_2$-TPR

Different reducibility of the various Cu sites present in Cu-SSZ-13 makes $H_2$-TPR a useful characterization method for investigating the relative distribution of these sites. Fig. 2 shows the $H_2$-TPR and component-deconvolution profiles for the DG and FA Cu-SSZ-13 catalyst samples. The TPR profiles of Fig. 2 represent reduction of Cu(II) to Cu(I), which is relevant to SCR as the underlying redox half reactions cycle the Cu inventory between Cu(II) and Cu(I). The TPR profile of the DG catalyst can be deconvoluted into two peaks with maxima at ca. 250 °C and 350 °C, which are associated with reduction of $Z_1$CuOH and $Z_2$Cu sites, respectively [12,15,28]. The areas under these component profiles suggest that the DG sample has 70% of the Cu sites in $Z_1$CuOH form and 30% as $Z_2$Cu. The FA TPR profile has three component features with maxima at 250 °C, 390 °C and 470 °C, attributable to reduction of $Z_1$CuOH (or $CuO_x$), $Z_2$Cu, and sulfur sites (described below), respectively. As discussed later in Section 3.3, $^{29}$Si and $^{27}$Al NMR results show a slight dealumination of the SSZ-13 framework due to field aging, which could drive some isolated Cu ions out of the framework and form $CuO_x$ clusters. As shown by Gao et al., these $CuO_x$ clusters have a reduction peak around the same temperature as $Z_1$CuOH [29], making the exact
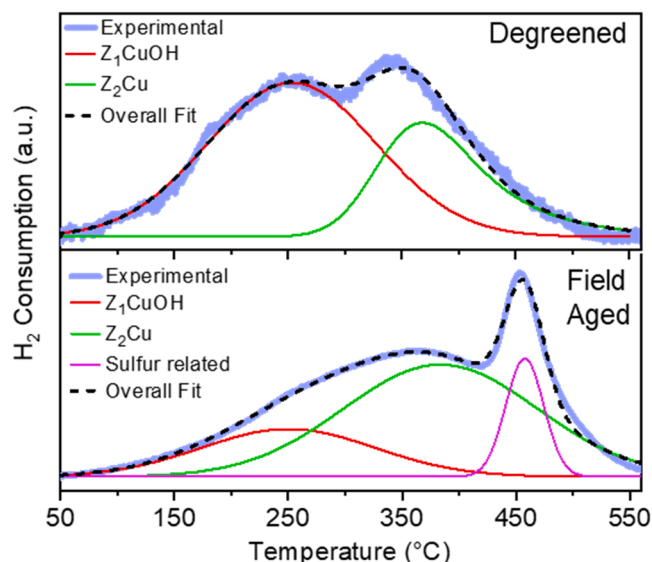
**Fig. 2.** $H_2$ TPR profiles of the DG and FA Cu-SSZ-13 samples, and corresponding component deconvolution results.

quantification of $Z_1CuOH$ fraction in the FA sample difficult. Area analysis suggest that the FA catalyst has 30% of total Cu sites in $Z_1CuOH$ and $CuO_x$ form and 70% as $Z_2Cu$. Similar $Z_1CuOH$ and $Z_2Cu$ distributions were also shown by T-O-T bond vibrations of $NH_3$ saturated Cu-SSZ-13 collected using DRIFTS (see Fig.S1c in Supplementary file). The FA catalyst undergoes hydrothermal aging (HTA) during its on-road lifetime, and several studies have presented evidence that HTA converts $Z_1CuOH$ to $Z_2Cu$ [3,12,30,31]. Luo et al. proposed the following reaction for such Cu-inventory changes [12]:

$$Z_1CuOH + ZH \rightarrow Z_2Cu + H_2O \qquad (1)$$
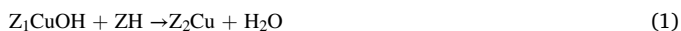
Eq. (1) indicates that the $Z_1CuOH$-to-$Z_2Cu$ transformation associated with FA also consumes some Bronsted acid sites (ZH); $NH_3$ TPD results discussed later show direct experimental evidence of this. To understand the origin of the 470 °C peak in Fig. 2(b), a mass spectrometer was used to monitor $m/z = 2$ ($H_2$) and $m/z = 64$ ($SO_2$ & $H_2SO_4$) signals during the TPR experiment. Fig. S1 of the Supplementary file shows distinct consumption and production peaks in the $m/z = 2$ and $m/z = 64$ signals, respectively, at 470 °C, and indicates that the corresponding TPR peak in Fig. 2 is due to $H_2$ consumption by sulfur containing species.

### 3.2. ICP and sulfur-species TPD

Catalysts are typically exposed to fuel-born sulfur impurities during their on-road lifetimes. Some of these sulfur species strongly adsorb to the catalyst and poison the SCR active sites [14–16,32]. Table 1 shows the results of elemental analysis of the DG and FA catalyst samples (crushed monolith including catalyst washcoat) using ICP. The total Cu weight percent in both samples are similar indicating that physical loss of Cu via erosion or leaching did not occur during field aging. While there was no sulfur present in the DG catalyst, 0.41 wt% sulfur was

**Table 1**
Elemental analysis of DG and FA catalyst samples using ICP. Weight percent values are normalized to washcoat loading using ICP-measured Mg as a cordierite monolith indicator.

| Element | Catalyst (Component weight %) | |
|---|---|---|
| | DG | FA |
| Cu | 2.5 | 2.4 |
| S | 0 | 0.41 |
| P | 0 | 0.26 |

detected in the FA sample, which results in an S:Cu molar ratio of 0.34:1 (weight ratio of 0.41: 2.4) meaning that 34% of Cu sites in FA catalyst could be poisoned by sulfur if the Cu-S coordination is unity. Literature suggests that the interactions of $Z_1CuOH$ and $Z_2Cu$ sites with sulfur are not similar and their desulfation temperature vary [15]. As discussed below, sulfur-species TPD was performed to investigate the distribution of sulfur among the various FA-catalyst sites. Phosphorus (originating from lubricant oil) was also detected on the FA catalyst which could negatively affect SCR performance [33]. Impact of phosphorus on the active sites is not well understood and is the focus of our ongoing studies.

Adsorbed sulfur-containing species on the FA catalyst were studied via TPD by monitoring $m/z = 64$ signal while heating from room temperature to 1000 °C at a ramp rate of 10 °C/min. The TPD profile in Fig. 3 shows that no sulfur-related species are desorbed below 400 °C, and deconvolution indicates four major sulfur components with desorption peaks, centered around 490 °C, 590 °C, 680 °C and 880 °C. Deconvolution using only three peaks and neglecting the copper sulfates (680 °C feature) resulted in a poor fit as shown in Fig. S2. From their experimental work and density functional theory (DFT) calculations on sulfated Cu-SSZ-13 samples, Jangjou et al. showed that $H_2O$-solvated $Z_2Cu$ sites adsorb sulfur mainly as ammonium sulfate ($(NH_4)_2SO_4$) [15]. As this sulfur-adsorption pathway requires $NH_3$, and since $NH_3$ is always present during SCR operation in on-road applications, ammonium sulfate coordinated with $Z_2Cu$ is expected to form on FA catalysts. Indeed, the peak at 490 °C can be assigned to ammonium sulfate, as also reported by Xi et al. and Mesilov et al. [14,32]. Sulfur adsorbs to the $Z_1CuOH$ sites both in the presence and absence of $NH_3$, although $NH_3$ can enhance adsorption capacity; it can occur under dry conditions, and exists in bisulfite form shown in Eq. 2 [15].

$$Z_1CuOH + SO_2 \rightarrow Z_1CuHSO_3 \qquad (2)$$

Copper bisulfite desorbs at a higher temperature than ammonium sulfate, and the second TPD peak at 590 °C in Fig. 3 can be assigned to bisulfites [14,15,32]. Bisulfites can further oxidize to bisulfates and sulfates in the presence of $O_2$ as reported by Mesilov et al. and Jangjou et al. [15,32], and shown in Eqs. (3) and (4), respectively.
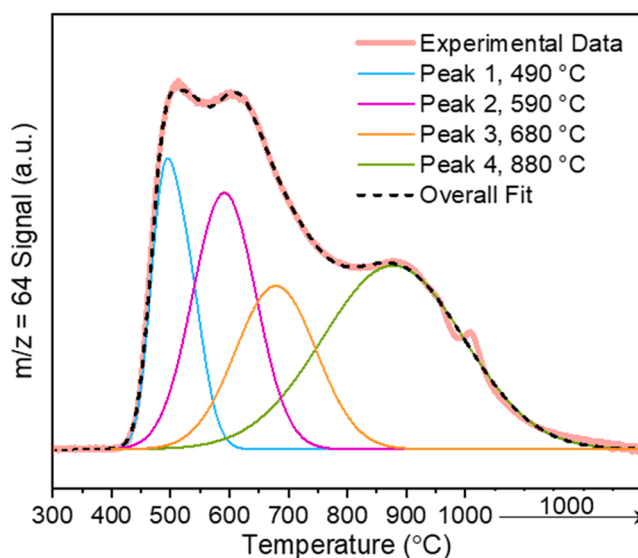
$$Z_1CuHSO_3 + 1/2\, O_2 \rightarrow Z_1CuHSO_4 \qquad (3)$$



**Fig. 3.** $SO_2$ ($m/z = 64$) released during TPD of the FA Cu-SSZ-13 under inert flow. Associated peak deconvolution is also shown in the figure. The deconvolved features are assigned as 490 °C to ammonium sulfate on $Z_2Cu$, 590 °C to bisulfite on $Z_1Cu$ ($Z_1CuHSO_3$), 680 °C to copper sulfates via a $Z_1Cu$ intermediate, and 880 °C to aluminum sulfates with contributions from $CuSO_4$ decomposition in the low-temperature regions.

$$Z_1CuHSO_3 + 1/2 O_2 \rightarrow ZH + CuSO_4 \tag{4}$$

In on-road field operation, catalysts are subjected to high oxygen concentrations, which makes formation of sulfates possible. Xi et al. assigned TPD peaks in the 500–800 °C range to decomposition of copper sulfates [14], indicating that the third TPD peak centered around 680 °C is associated with copper sulfates on the FA catalyst. When the Cu-SSZ-13 catalyst is heated above 800 °C, dealumination and deterioration of the zeolite structure takes place which could modify the interactions between sulfur species and aluminum and thereby lead to formation of aluminum sulfates, which decompose at temperatures as high as 920 °C [14,34]. Moreover, the washocoated catalyst contains alumina as a binder which could react with sulfur oxides to form aluminum sulfate. The fourth TPD peak centered around 880 °C in Fig. 3 thus is a result of aluminum sulfate decomposition. Since this peak is quite broad (starting around 500 °C), the lower-temperature portion may have contributions from $CuSO_4$ decomposition. In summary, the TPD features in Fig. 3 at 490 °C, 590 °C, 680 °C, and 880 °C, are associated with ammonium sulfate on $Z_2Cu$, bisulfite on $Z_1Cu$ ($Z_1CuHSO_3$), copper sulfates via a $Z_1Cu$ intermediate, and aluminum sulfate, respectively.

The total area under the TPD peaks at 590 °C and 680 °C is 2.5 times higher than the area under the peak at 490 °C, indicating that the $Z_1CuOH$ sites adsorb correspondingly more sulfur than the $Z_2Cu$ sites. Considering further that only 30% of the total Cu sites of the FA sample are of $Z_1CuOH$ form (Fig. 2, Section 3.1), this shows that the $Z_1CuOH$ sites adsorb sulfur at a much higher S:Cu ratio than the $Z_2Cu$ sites.

### 3.3. $^{29}$Si and $^{27}$Al NMR

During real-world driving condition, the Cu-SSZ-13 catalyst is exposed to high temperatures for extended time periods which could result in dealumination of framework aluminum. This decreases the number of exchange sites available for Cu, and therefore can result in a loss of exchanged isolated Cu sites and Bronsted acid sites. Possible dealumination in the DG and FA catalyst samples was studied using $^{29}$Si and $^{27}$Al solid-state NMR, and the respective spectra are shown in Fig. 4 (a) and (b). The DG catalyst shows three $^{29}$Si spectral features at



**Fig. 4.** (a) $^{29}$Si and (b) $^{27}$Al solid-state NMR spectra of the DG (green spectra) and FA (red spectra) catalysts.

−111 ppm, −106 ppm and −101 ppm; these resonances can be assigned to Si surrounded by 4 Si, 3 Si 1 Al (3 Si atoms and 1 Al atom), and 3 Si 1 OH, respectively [35–37]. The −111-ppm peak is a characteristic of tetrahedral zeolite framework, the −106-ppm peak arises from the presence of framework Al, and the −101-ppm peak is due to $SiO_4$ tetrahedra containing a connected OH group. Dealumination process would lead to a decrease in the −106 ppm and −101 ppm peaks relative to the −111 peak; loss of framework Al reduces the charge imbalance that creates the OH exchange sites, and thus dealumination leads to loss of the −101-ppm $^{29}$Si feature. Indeed, the FA-sample spectra shows decreased relative intensities of the −106-ppm and −101-ppm features, indicating a certain degree of dealumination of the framework aluminum. The $^{27}$Al NMR spectra of Fig. 4(b) exhibit two main peaks at 57 ppm and 8 ppm for both the DG and FA catalysts. The 57-ppm peak is attributable to tetrahedral Al in the zeolite framework, and the 8-ppm peak to octahedral Al in the $Al_2O_3$ binder present in these samples [38–40]. The FA sample spectra also contains a third feature at 38 ppm that is assigned to five-coordinated extra-framework Al created by dealumination [40]. While cordierite can contribute a 38-ppm peak, its absence from the DG-sample results indicates that the sample-preparation method resulted in negligible cordierite impurities in the analyzed DG and FA samples, and thus the 38-ppm peak for FA-sample analysis is mainly associated with extra-framework Al. Dealumination should also lead to a peak in the 0–10 ppm range arising from octahedral Al; however, this region suffers resonant interference from $Al_2O_3$ binder in the case here. Both the $^{29}$Si and $^{27}$Al NMR results show consistent and independent evidence that field aging leads to dealumination of the SSZ-13 zeolite framework, which can change the Lewis and Bronsted acid site distributions and thereby affect the SCR performance and redox half cycles.

### 3.4. Reducible-Cu density

Sulfur adsorption on isolated Cu sites and dealumination-induced loss of exchanged Cu ions can result in a loss of reducible Cu. To investigate such changes, the RHC-a step of the TRCR protocol was used to calculate reducible Cu density of both the DG and FA samples. The RHC-a step involves reduction of Cu(II) sites to Cu(I) via reaction with $NO+NH_3$ and formation of $N_2$ product. The number of Cu sites reduced is equimolar to the number of $N_2$ molecules formed [25–27], and therefore the area under the RHC-a $N_2$ transient is a measure of the number of reducible Cu in the sample [19]. Fig. 5 shows the calculated reducible-Cu density of the DG and FA catalysts as functions of temperature and intra-catalyst location. As expected, the reducible-Cu density of the FA catalyst is lower than that of the DG catalyst for all the temperatures and intra-catalyst locations. At 200 °C and 1/8 L, the DG sample contains around 37 mmol/L of reducible Cu compared to only 24 mmol/L (35% lower) for the FA catalyst; this is a consequence of sulfur aging, hydrothermal aging and dealumination occurring during field operation. With increasing temperature, reducible-Cu density in the DG catalyst shows a decreasing trend. Prior to $NH_3$ introduction at RHC-a onset, the catalyst is exposed to NO, and the literature has shown that NO alone can partially reduce Cu [25]. As shown in our earlier publication, such Cu pre-reduction preceding RHC-a increases with temperature and leads to decreasing reducible-Cu count [19]. Moreover, a small fraction of Cu species can be oxidized by $H_2O$ and impurity $O_2$ in the gas stream. Due to a combination of these factors, measured reducible-Cu density decreases with increasing temperature. Interestingly, the reducible-Cu density in the FA catalyst remains constant with temperature, which indicates that the FA catalyst has lower activity for pre-reduction of Cu by NO as well as for oxidation of Cu by $H_2O$ and $O_2$. Consequently, the gap between the reducible-Cu densities of the DG and the FA samples narrows with increasing temperature, and becomes 22% at 1/8L and 450 °C.
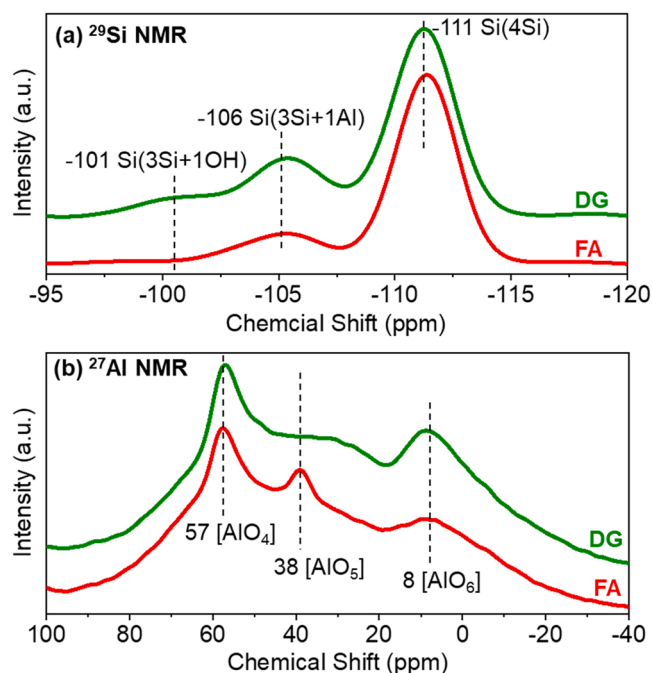
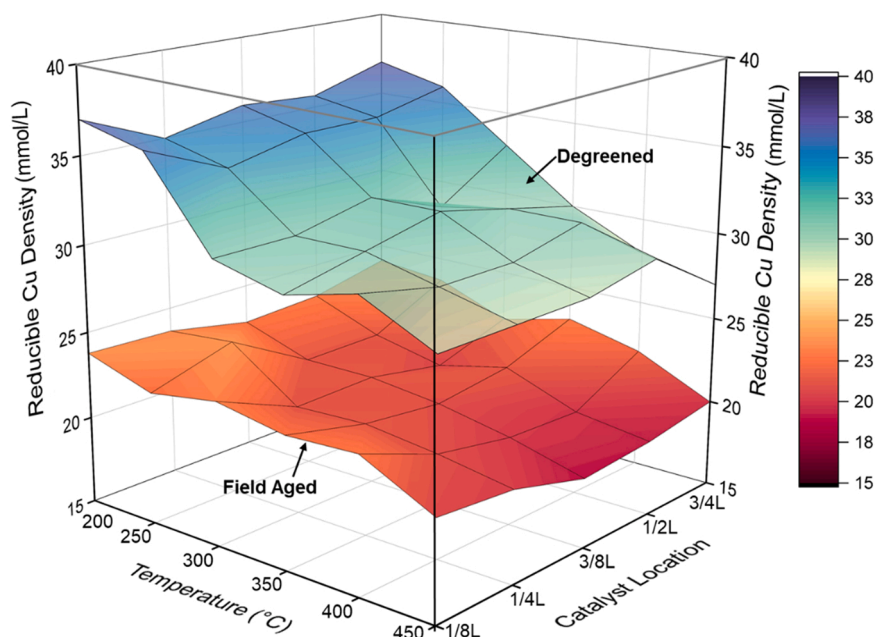**Fig. 5.** Reducible-Cu density of the DG and FA catalysts at various intra-catalyst locations and operating temperatures.

## 3.5. NH₃ TPD

The NH₃ storage capacity is an important property of SCR catalysts, and NH₃ stored on both Lewis-acid and Bronsted-acid sites can contribute towards the overall SCR reaction. The NH₃-capacity of a catalyst sample and its partitioning between Lewis- and Bronsted-acid sites can be quantified via NH₃ TPD of an NH₃-saturated sample. Fig. 6 shows that the NH₃ TPD profiles of the DG and FA Cu-SSZ-13 samples contain two distinct peaks centered at 320 °C and 430 °C, which are related to NH₃ desorption from Lewis- and Bronsted-acid sites, respectively [3,13,30,31]; the higher binding strength of NH₃ on Bronsted-acid sites results in a higher desorption temperature [31]. Deconvolution of the Lewis- and Bronsted-site contributions to the overall TPD is shown in Fig. S3, and the corresponding areas were used to determine total NH₃ capacity along with that of each acidic site as shown in Table 2. Field aging results in a 44% (33 mmol/L) loss of NH₃ capacity relative to the DG state; 82% (27 mmol/L) of this NH₃ capacity loss is associated with field aging impact on the Bronsted acid sites, and only 18% (6 mmol/L) with that on the Lewis acid sites. Field aging is a
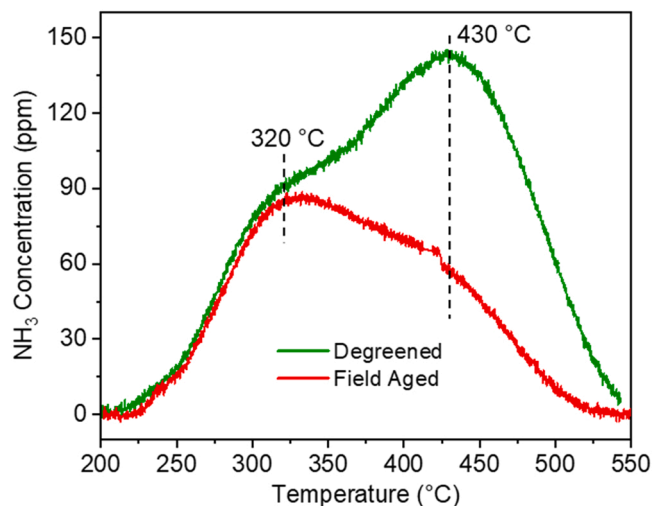
**Table 2**

Total NH₃ released (indicating chemisorbed NH₃ capacity) during TPD, and partitioning of the chemisorbed NH₃ capacity between the Lewis-acid and Bronsted-acid sites, of the DG and FA Cu-SSZ-13 catalysts.

| Catalyst | NH₃ released (mmol/L) | | |
|---|---|---|---|
| | Total | Lewis-site bound | Bronsted- site bound |
| Degreened | 74 | 26 | 48 |
| Field Aged | 41 | 20 | 21 |

complex process comprised mainly of HTA and sulfur aging. In general, mild hydrothermal aging converts $Z_1CuOH$ sites to $Z_2Cu$ while consuming Bronsted-acid sites in the process and conserving the total reducible Cu [12], while severe hydrothermal aging could lead to dealumination and subsequent loss of ion exchanged Cu sites. Despite literature indicating that the NH₃ capacity of $Z_2Cu$ is twice that of $Z_1CuOH$ [30,31], and that the FA catalyst contains a higher $Z_2Cu$ fraction than the DG catalyst (see Fig. 2 and Section 3.1), the FA catalyst nevertheless exhibits a smaller 320 °C peak than the DG catalyst (see Fig.S3). This net loss of NH₃ desorption from Lewis-acid sites (Table 2) with field aging indicates a net decrease in the Cu sites available on the FA sample, likely due to sulfur aging and dealumination, and is consistent with the reducible-Cu density calculations discussed in Section 3.4. Loss of total NH₃ capacity and reducible-Cu density in the FA sample can degrade SCR activity.

## 3.6. Integral NO SCR and NH₃ oxidation activity

To ensure that emission levels meet environmental regulations over a range of operating conditions and extended time period, the volume of commercial catalyst monoliths are larger than required for complete NO conversion with a new catalyst and under less-challenging operating conditions; the extra catalyst volume, not used when new and under less-challenging conditions, provides a buffer to address aging and more-challenging operating conditions and improves catalyst durability and lifetime. Whether spatially uniform or localized, aging degrades catalyst activity, requiring a greater catalyst volume to achieve the same conversion compared to its fresh state. In addition to catalyst-exit or integral performance, understanding how the distribution of various



**Fig. 6.** NH₃ TPD profiles of the DG and FA Cu-SSZ-13 catalysts.

catalyst functions and reactions are impacted by ageing and operating conditions is useful for designing robust and durable catalyst systems. This section discusses the overall integral SCR activity of the DG and FA catalyst cores, while variations in intra-catalyst performance are discussed in Section 3.7.

The integral NO conversions achieved from 1-inch long cores of the DG and FA catalysts are shown in Fig. 7(a). The DG catalyst shows 95% NO conversion at 200 °C, complete conversion in the 250–350 °C range, and progressively degrading conversion above 350 °C primarily due to parasitic $NH_3$ oxidation by $O_2$. Kamasamudram et al. defined parasitic oxidation of $NH_3$ as any reaction that causes an imbalance between $NO_x$ and $NH_3$ conversions during SCR across a wide temperature range (200–600 °C); at lower temperatures, such $NH_3$ oxidation occurs by reaction with $NO_2$ or surface sites oxidized by $NO_2$, while the parasitic oxidation at higher temperatures occurs by reaction with $O_2$. Direct $NH_3$ oxidation by $O_2$ (in the absence of NO) is discussed in relation to Fig. 7 (b). Integral NO conversion of the FA catalyst is similar to the DG state except at 200 °C, where it is (82%) 14% lower. This lower 200 °C conversion is a major concern as it causes increased cold-start emissions. Both HTA and sulfur aging may contribute to this loss of low-temperature SCR activity [3,14–17]. Luo et al. have shown that the low-temperature SCR $NO_x$ conversion on Cu-SSZ-13 catalysts decreases continuously with increasing HTA temperature [3]. The impact of sulfur poisoning on low-temperature SCR activity of Cu-SSZ-13 has been studied by Xi et al., Shih et al. and Jangjou et al. [14–16]. All these studies show that sulfur poisoning decreases SCR activity, mainly due to the lower mobility of sulfated-Cu species compared to non-sulfated Cu species. The degraded low-temperature SCR performance of the FA catalyst is apparently a combined impact of HTA and sulfur aging; we are currently working to untangle these component impacts of FA, and

plan to publish those studies separately.

Fig. 7(b) shows $NH_3$ oxidation with $O_2$ for the DG and FA catalysts, which can compete with and degrade the overall SCR efficiency, and Fig. S4 shows that practically all of the oxidized $NH_3$ forms $N_2$ product. The DG catalyst exhibits higher $NH_3$ oxidation activity than the FA catalyst. Luo et al. have shown that $NH_3$ oxidation activity of Cu-SSZ-13 decreases with increased HTA temperature [3]. They used $NH_3$ TPD and DRIFTS to conclude that $Z_1CuOH$ sites have higher $NH_3$ oxidation activity than $Z_2Cu$ sites. Since the FA catalyst has lower $Z_1CuOH$ fraction compared to the DG catalyst (see Fig. 2), it makes sense that it also has lower $NH_3$ oxidation activity. While direct and parasitic $NH_3$ oxidation can differ [41], in general lower $NH_3$ oxidation improves $NH_3$ utilization during SCR. Since a larger fraction of $NH_3$ is available for SCR reaction on the FA catalyst from 250 °C to 450 °C, the $NH_3$ dosing per NO converted can theoretically be lower than that for the DG catalyst, which needs greater than stoichiometric $NH_3$ to account for the loss by oxidation.

### 3.7. Field aging impacts on RHC and OHC based on the TRCR protocol

Even before combining with kinetic models to determine half-cycle kinetic parameters, the experimental TRCR protocol measurements at intra-catalyst locations provide quantitative insights of how field aging impacts RHC and OHC. Intra-catalyst measurements are specifically relevant to transient CI studies of half-cycle balancing as these are most distinct at the catalyst front and degrade along the catalyst length as conversion progresses [21]. Moreover, integral conversion is ~100% in many cases, and intra-catalyst measurements are required to achieve fractional conversion suitable for half-cycle kinetic-model fitting. In this section, we discuss insights obtained from intra-catalyst TRCR-protocol measurements regarding the effect of field aging on SCR Cu-redox half-cycle kinetics.

Fig. 8(a)–(c) show SCR $N_2$ formation as a function of fractional catalyst length (0 L: catalyst inlet, 1 L: catalyst exit) at 200 °C, 300 °C and 400 °C. Since the selectivity towards $N_2O$ and $NO_2$ is low at the catalyst exit (Fig. S5 in the Supplementary file), such $N_2$ measurement can also be viewed as the total amount of NO converted. At each temperature, $N_2$ formation in the front catalyst-half (<1/2 L) is lower for the FA catalyst than the DG catalyst. At 200 °C, the FA catalyst's $N_2$ formation is substantially lower than that from the DG catalyst throughout the entire catalyst length. In fact, within the first catalyst-half, this difference at 200 °C is almost 50%, indicating a two-fold decrease in SCR performance due to field aging. In the second catalyst-half (>1/2 L), the SCR-activity difference at 200 °C decreases and becomes ca. 30% at 3/4 L. The DG catalyst has high conversion in this second catalyst-half, leaving little NO and $NH_3$ remaining and correspondingly decreasing the DG SCR rate. On the contrary, the FA catalyst has much lower SCR conversion in the first catalyst-half, leaving more reactants in the second half, which causes greater relative SCR rate for the FA catalyst, thus decreasing the SCR-conversion differences between the two samples. At 300 °C, 100% NO conversion is achieved by 3/8 L for the DG catalyst and ~1/2 L for the FA catalyst. Like at 200 °C, the 300 °C SCR-conversion differences between the two catalysts decreases along catalyst length as conversion progresses and becomes negligible where both catalysts achieve complete NO conversion. Thus, although both catalysts achieved complete integral NO conversion, the FA catalyst requires a greater catalyst fraction or length. In general, SCR progressively slows along the catalyst length as conversion increases and stops at the point of complete conversion. Similar trends are observed at 400 °C, where conversion plateaus and converges for the DG and FA catalysts; in this case SCR is limited to ~95% conversion due to $NH_3$ oxidation as discussed in Section 3.6. Therefore, field aging decreases the SCR activity of the Cu-SSZ-13 catalyst throughout the entire temperature range and increases the catalyst length needed for matching the conversion achieved in DG catalyst. Higher relative reaction rates with increasing temperature shortens this required reaction zone, thereby allowing
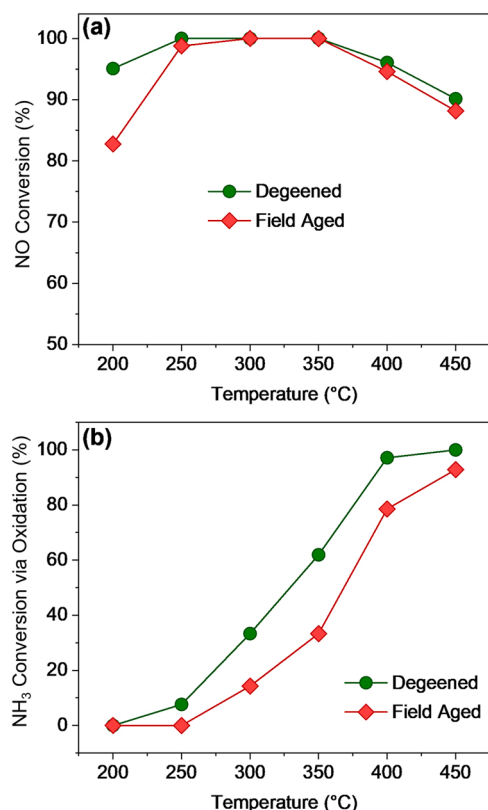


**Fig. 7.** (a) Integral NO conversion of the DG and FA catalyst samples at SS Standard SCR reaction. Reaction conditions: 200 ppm NO, 200 ppm $NH_3$, 5% $H_2O$, 5% $O_2$, balance Ar, 40,000/h space velocity. (b) Integral $NH_3$ conversion during SS oxidation by $O_2$. Reaction conditions: 200 ppm $NH_3$, 5% $O_2$, 5% $H_2O$, balance Ar, 40,000/h space velocity.
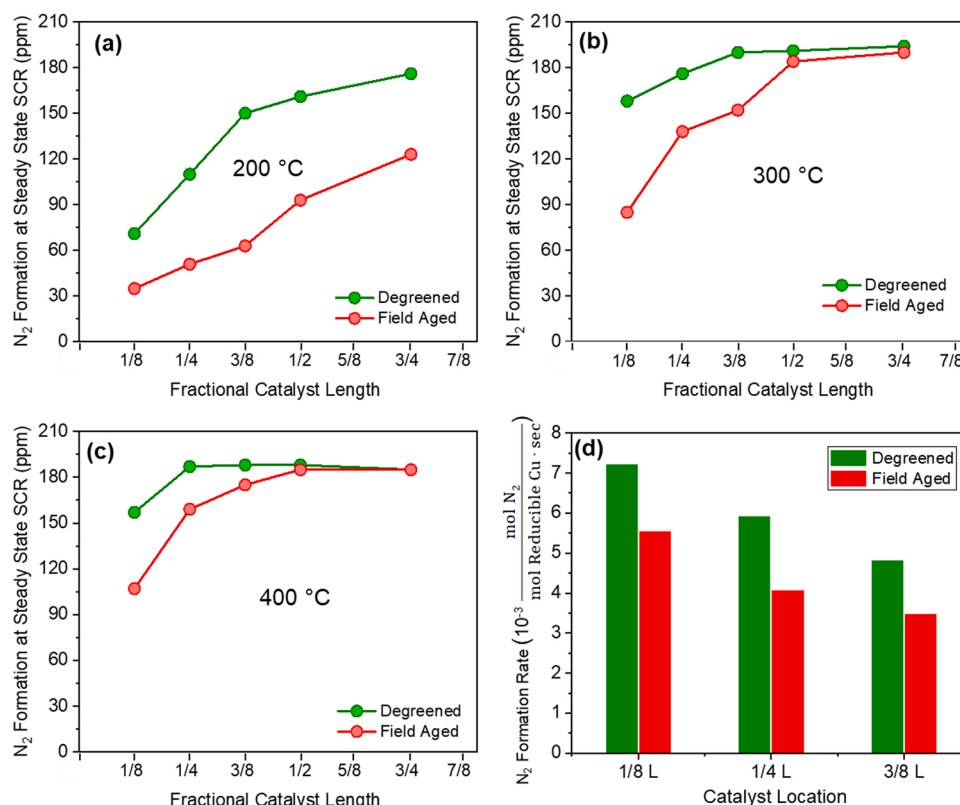
**Fig. 8.** Intra-catalyst $N_2$ formation during SS SCR at various intra-catalyst locations at (a) 200 °C, (b) 300 °C and (c) 400 °C. Reaction conditions: 200 ppm NO, 200 ppm $NH_3$, 5% $H_2O$, 5% $O_2$, balance Ar, 40000/h space velocity. (d) Intra-catalyst $N_2$ formation normalized by reducible Cu during SS SCR at 200 °C and various intra-catalyst locations.

complete NO conversion within the full catalyst core.

The degraded global SCR rate of the FA catalyst apparent in Fig. 8 could have various origins, including but not limited to, loss of active-Cu sites and impact on the individual half-cycle rates. As discussed in Section 3.4, adsorption of sulfur-based species on Cu sites leads to a loss in the reducible-Cu density during field ageing. Such a loss of active-Cu sites is a major reason for the FA catalyst's degraded SCR activity. However, based on Fig. 8(d), which shows the SS-SCR $N_2$ formation rate at 200 °C with the DG and FA catalysts normalized by their reducible-Cu density, it appears that loss of active-Cu sites is not the sole reason behind SCR activity degradation in the FA catalyst. Fig. 8(d) shows that the FA catalyst has 30–40% lower $N_2$ formation rate per reducible-Cu site compared to the DG catalyst, at a range of intra-catalyst locations and effective space velocities. Had Cu-site loss been the sole origin of

SCR-activity loss without any changes in the half cycle kinetics, there should have been no significant changes in the normalized $N_2$ formation rate at SS SCR. This indicates that field aging also affects the SCR half-cycle rates in a way that needs detailed investigation and understanding. The remainder of this paper focuses on elucidating how field aging impacts the individual half-cycle rates and whether these impact RHC and OHC equivalently or selectively.

The impact of field aging on the individual half-cycle rates can be determined from the CI heights of the TRCR-protocol SCR steps. Fig. 9(a) shows the SCR-b and SCR-c CI transients at 3/8 L within the DG catalyst, and as discussed in Section 2.4, these CI peak heights provide a measure of the OHC and RHC rate, respectively. The SCR-b CI has a lower height than the SCR-c CI for the DG catalyst at 200 °C, indicating a slower OHC than RHC. However, at 250 °C the DG catalyst's CI heights have
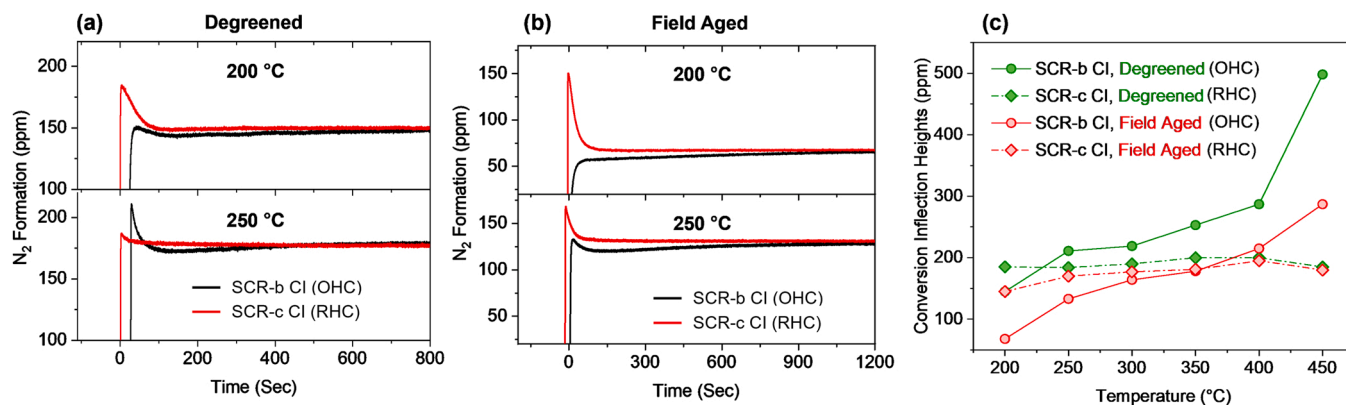


**Fig. 9.** SCR-b and SCR-c conversion inflections at 3/8 L, and 200 °C and 250 °C for (a) DG catalyst and (b) FA catalyst. (c) Conversion-inflection heights of the SCR-b and SCR-c steps at 3/8 L for the two catalysts at a range of temperatures. The half cycle controlling the CI onset is noted parenthetically in the legends.

opposite behavior, indicating that the OHC rate is faster than the RHC rate. Thus for the DG catalyst, OHC has a more rate-limiting effect than RHC on the SCR reaction at 200 °C, while the RHC has a stronger limiting effect on SCR at 250 °C, suggesting that the OHC kinetics increases faster with temperature than do the RHC kinetics. Fig. 9(b) shows that 3/8 L within the FA catalyst, RHC is much faster than OHC at 200 °C, and that while both half-cycle rates increase at 250 °C, RHC remains faster than the OHC. Thus, OHC has a stronger limiting effect on SCR for the FA catalyst at both temperatures; this is different from the DG-catalyst nature, and suggests that field aging selectively degrades the OHC rate.

The selective impact of field aging on OHC is further apparent by plotting the half-cycle rates, as determined by the SCR-b and SCR-c CI heights, over a broader temperature range for the DG and FA catalysts, as shown for 3/8 L in Fig. 9(c). The RHC rates (SCR-c CI) are a weak function of temperature for both catalyst states. The OHC rate (SCR-b CI) increases with temperature for the DG catalyst, and dramatically so at the low- and high-temperature points; the FA catalyst's OHC rate has a similarly shaped temperature dependence, but with significantly less increase at the highest temperature. Compared to the DG catalyst, the FA catalyst has only slightly lower RHC rate and much greater OHC-rate degradation across the investigated temperature range. The crossover temperature where OHC rate exceeds the RHC rate shifts from ~230 °C for the DG catalyst to ~350 °C for the FA catalyst. All of these features demonstrate that field aging selectively impacts OHC to a greater degree than RHC.

The minor impact of field aging on RHC can also be verified by comparing RHC transients from the DG and FA samples. Fig. 10(a) shows the RHC-c $N_2$-formation rate normalized by the corresponding reducible Cu at 1/8 L of both the DG and FA catalysts at 200 °C. The transient curves are similar for both catalysts, indicating that RHC is minimally impacted by field aging, which is consistent with the RHC conclusions from Fig. 9(c). In Section 3.8, we delve further into these RHC-c $N_2$ transients using kinetic modelling and show that RHC-rate parameters are not impacted appreciably by field aging.

The Cu(II) fraction at SS SCR provides additional experimental evidence of the selective impact of field aging on OHC beyond that apparent in Fig. 9(c). The Cu(II) fraction at SS SCR provides a measure of the relative RHC and OHC kinetics. A greater or lesser Cu(II) fraction indicates faster or slower relative OHC, respectively, and vice versa for RHC. Fig. 10(b) show the Cu(II) percentage during SS SCR at 1/8 L location on the DG and FA catalysts at various temperatures. This Cu(II) fraction for both catalysts increases with temperature suggesting faster OHC at higher temperatures. This is consistent with Fig. 9(c) which showed the OHC rate to increase with temperature while RHC remained relatively constant for both catalyst samples. More relevant to aging, Fig. 10(b) also shows that this Cu(II) fraction is lower for the FA catalyst than the DG catalyst at all temperatures, indicating that field ageing slows the OHC kinetics more than the RHC kinetics. This independent analysis of the TRCR-protocol data indicates that field aging of Cu-SSZ-13 in SCR applications selectively slows the OHC and has minimal impact on the RHC, which is consistent with similar analysis of Fig. 9(c).

While such TRPR-protocol analysis provides a quantitative measure of how field aging impacts the individual half cycles, further insights are available by combining this data with kinetic models in a transient-response methodology to determine how the RHC and OHC kinetic parameters are impacted by aging, which is the focus of the next two sections.

### 3.8. Field aging impact on RHC kinetics

This section focuses on determining RHC kinetic parameters and how they are impacted by ageing via the transient-response methodology as described in Section 1, where a kinetic model is fit using the TRCR-protocol transient data.

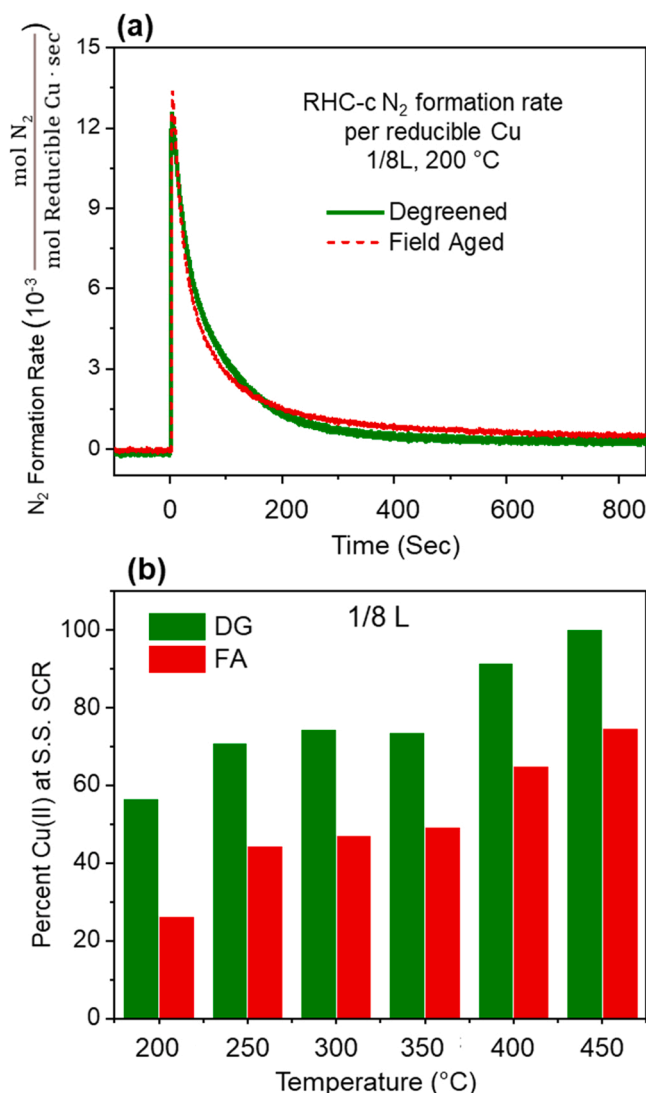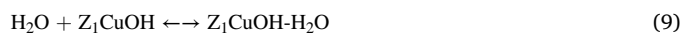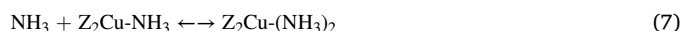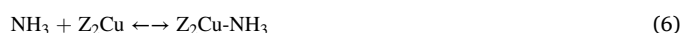An NH$_3$-adsorption model was adopted based on the work of



**Fig. 10.** (a) RHC-c transient $N_2$-formation rate normalized by reducible Cu for the DG and FA catalysts at 200 °C and 1/8 L. (b) Cu(II) percentage at SS SCR calculated from the TRCR protocol RHC-b step for the DG and FA catalysts at 1/8 L.

Ladshaw and Pihl [42]. In that work, the NH$_3$ adsorption on Cu-SSZ-13 was comprised of NH$_3$ adsorption-desorption reactions on three distinct sites, and included two reactions for competitive adsorption by water vapor.
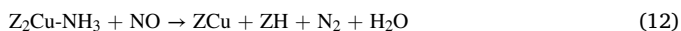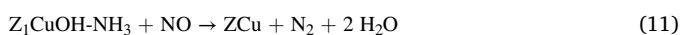
$$NH_3 + Z_1CuOH \longleftrightarrow Z_1CuOH\text{-}NH_3 \tag{5}$$

$$NH_3 + Z_2Cu \longleftrightarrow Z_2Cu\text{-}NH_3 \tag{6}$$

$$NH_3 + Z_2Cu\text{-}NH_3 \longleftrightarrow Z_2Cu\text{-}(NH_3)_2 \tag{7}$$

$$NH_3 + ZH \longleftrightarrow ZNH_4 \tag{8}$$

$$H_2O + Z_1CuOH \longleftrightarrow Z_1CuOH\text{-}H_2O \tag{9}$$

$$H_2O + Z_2Cu \longleftrightarrow Z_2Cu\text{-}H_2O \tag{10}$$

Reaction 5 represents NH$_3$ adsorption and desorption from Z$_1$CuOH sites. Luo et al. performed a comprehensive work using H$_2$-TPR, DRIFTS and NH$_3$ TPD to conclude that Z$_1$CuOH sites can accommodate one NH$_3$ molecule, while Z$_2$Cu sites can adsorb up to two NH$_3$ molecules [12]. They also reported that Bronsted acid sites accommodate one NH$_3$ molecule. In subsequent publications, Daya et al. used these Cu-site NH$_3$ co-ordinations in their NH$_3$-capacity model and two NH$_3$ on Bronsted
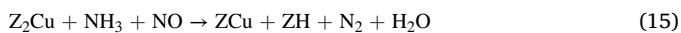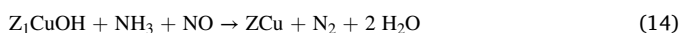
acid sites, and obtained great agreement between their model predications and experimentally obtained $NH_3$ breakthrough and TPD curves [30,31]. Since the catalyst samples used in the current study are similar commercial samples as used by Luo et al., we also assumed one $NH_3$ co-ordination for $Z_1CuOH$ sites. Reactions 6 and 7 represent $Z_2Cu$ sites adsorbing one and two $NH_3$ molecules, respectively. Moreno-González et al. also showed via EPR studies that $Z_2Cu(NH_3)_2$ is the most stable Cu-amine complex in the double 6-membered ring at 150 °C, and that subsequent $NH_3$ desorption leads to the stabilization of $Z_2Cu(NH_3)$ at 250 °C [43]. Note that $NH_3$-coordinations of 3 and 4 for $Z_1CuOH$ and $Z_2Cu$ has been suggested in the literature by DFT studies [9,44]; however, such high $NH_3$ co-ordination is unlikely at temperatures above 200 °C on the commercial catalyst used in this study, as shown by Daya et al. [31]. Reaction 8 accounts for adsorption of one $NH_3$ molecule per Bronsted-acid site. In their computational study, Paolucci et al. reported that $H_2O$ molecules also can adsorb on the isolated Cu sites [9]. The current study is performed under 5% $H_2O$, and therefore, $H_2O$ adsorption on $Z_1CuOH$ and $Z_2Cu$ sites is considered via Reactions 9 and 10, respectively [42].

Two different pathways for NO and $NH_3$ reaction during RHC-c were considered in the model. One set of reactions accounts for NO reaction with surface-adsorbed $NH_3$. Because $NH_3$ adsorption is reversible, in addition to the $NH_3$-coordinated Cu sites which participate in RHC via the surface-reactions pathway, a fraction of the sites remains $NH_3$ free at any given temperature. Such $NH_3$-free Cu sites can also participate in RHC by first activating NO molecules to form HONO or $H_2NNO$ intermediates, which then can react with gas-phase $NH_3$ to form $N_2$ and $H_2O$. A recent experimental and modeling study by Daya et al. reported existence of such gas-phase reactions [45]. A second set of reaction was consideredto accommodate this gas-phase RHC pathway.

Surface reactions:

$$Z_1CuOH\text{-}NH_3 + NO \rightarrow ZCu + N_2 + 2\ H_2O \quad (11)$$

$$Z_2Cu\text{-}NH_3 + NO \rightarrow ZCu + ZH + N_2 + H_2O \quad (12)$$

$$Z_2Cu\text{-}(NH_3)_2 + NO \rightarrow ZCu\text{-}NH_3 + ZH + N_2 + H_2O \quad (13)$$

Gas phase reactions:

$$Z_1CuOH + NH_3 + NO \rightarrow ZCu + N_2 + 2\ H_2O \quad (14)$$

$$Z_2Cu + NH_3 + NO \rightarrow ZCu + ZH + N_2 + H_2O \quad (15)$$

In Eqs 11–15, ZCu refers to a reduced Cu site, and ZH is a Bronsted acid site. Eqs. 11–13 show reactions between NO with $NH_3$ bound to $Z_1CuOH$ and $Z_2Cu$ sites. These Cu sites have been reported to have similar reduction kinetics [25,27], and thus, a single rate equation was used for the surface reactions:

$$r_{RHC,\ Surface} = k_{RHC,\ Surface} \bullet [NO] \bullet [Cu(II)\text{-}NH_3]^m,\ m{=}2 \quad (16)$$

where, $Cu(II)\text{-}NH_3$ is a general representation for $Z_1CuOH\text{-}NH_3$, $Z_2Cu\text{-}NH_3$ and $Z_2Cu\text{-}(NH_3)_2$, $r_{RHC,\ Surface}$ is the rate of surface reduction reactions, and $k_{RHC,\ Surface}$ is the corresponding rate constant. The order of reaction associated with $Cu(II)\text{-}NH_3$ is assumed as 2 in this model, i.e., $m = 2$; a second-order reaction with respect to Cu(II) is facilitated by the formation of two proximate $NH_3$-solvated Cu ions, as reported by Hu et al. in their experimental and computation work [25].

The gas-phase reactions occur on $NH_3$-free Cu sites, which cannot form di-nuclear complexes as proximate Cu ions lack mobility afforded by $NH_3$-solvation, and thus this pathway is assumed to be first order with respect to Cu(II).

$$r_{RHC,\ Gas} = k_{RHC,\ Gas} \bullet [NO] \bullet [NH_3] \bullet [Cu(II)]^n,\ n{=}1 \quad (17)$$

As with the surface reactions, Eq. (17) defines a single gas-phase reaction-rate constant for both $Z_1CuOH$ and $Z_2Cu$, where $r_{RHC,\ Gas}$ is the reaction rate and $k_{RHC,\ Gas}$ is the RHC rate constant.

The $NH_3$-capacity model and reduction-reaction networks were incorporated in a $^1D$–$^0D$ model to fit the experimentally measured $N_2$-formation transients like those in Fig. 10(a). The $^1D$–$^0D$ model is described further by Ladshaw and Pihl [42], as well as in the Supplementary file. Fig. 11(a) shows the experimental $N_2$ transient collected at 200 °C and 1/8 L, and the respective model fit. Excellent agreement between model-calculated and experimental transients was obtained at 200 °C, 250 °C and 300 °C (Fig. S6 and S7 in Supplementary file). The rate constants obtained from such model fits were then used to calculate the activation energies. Fig. 11(b) and (c) show the Arrhenius plots (ln (k) vs 1/T) of the surface and gas-phase reactions for the DG and FA catalysts, respectively. The RHC activation energies obtained from these plots are tabulated in Table 3, and are similar to those reported in the literature based on DFT calculations [44,46]. This more detailed transient-response analysis shows no significant differences in the activation energies of both the surface and gas-phase RHC routes for the DG and FA catalyst samples, indicates that field aging does not significantly alter the RHC energetics, and is consistent with the more basic TRCR-protocol analysis of Fig. 9(c).

### 3.9. Field aging impact on OHC kinetics

A similar experimental-modeling transient-response methodology as used to determine RHC kinetic parameters in Section 3.8, was also applied to determine OHC kinetic parameters and how they are impacted by field ageing. Because OHC can occur without producing an $N_2$ transient as for RHC (e.g., see Fig. 10(a)), an alternate approach was developed to discretely resolve the oxidation kinetics of Cu(I) ions, and this discrete transient was measured and fit using an OHC model to calculate rate parameters. To measure these oxidation kinetics, the Cu inventory was first completely converted to Cu(I) by NO+$NH_3$; this reduced Cu inventory was exposed to $O_2$ for a specific time period to oxidize a portion of the Cu(I) to Cu(II); this oxidized-Cu fraction was reduced by an NO+$NH_3$ mixture and the resulting $N_2$-product transient used to count the number of Cu(II) created in the discrete oxidation step. This sequence was repeated using progressively longer oxidation-step periods to discretely resolve the OHC transient. Fig. 12(a) shows the fraction of Cu(II) formed through the discretely resolved OHC transient on the DG and FA catalysts at 3/16 L and 1/4 L, respectively (locations with equivalent cumulative reducible Cu), and 200 °C, and simple curve fits to the discrete data to accentuate the trends. The FA catalyst has much slower Cu oxidation kinetics than the DG catalyst, confirming that field aging degrades the OHC kinetics.

The oxidation of Cu(I) during OHC can be expressed by the following rate equation:

$$R_{OHC} = k_{OHC} \bullet [O_2] \bullet [Cu(I)]^n, \quad (18)$$

where $R_{OHC}$ is the Cu(I) oxidation rate and $k_{OHC}$ is the associated rate constant. Because $O_2$ is in abundant excess (1.84 mmol/min) relative to the total reducible Cu (0.015 mmol) in these experiments, the $[O_2]$ can be assumed constant and combined into the rate constant:

$$R_{OHC} = k_{OHC,\ Global} \bullet [Cu(I)]^n \quad (19)$$

Because of the excess $O_2$ compared to the number of Cu oxidized, the integral OHC reaction is assumed to be within differential kinetic condition, and it is appropriate to fit the kinetic data using the rate equation (Eq. 18 and 19); vs. a full mass-transfer and kinetic model as would be required otherwise. Both first-order and second-order reaction ($n = 1$, 2) were evaluated during data fitting, and Fig. 12(b) shows these fits to the discrete DG-catalyst Cu-oxidation rate transient at 200 °C. It is clear from Fig. 12(b) that Cu oxidation follows a second-order dependance on Cu(I) concentration, and $n = 2$ was used for subsequent analysis. This is consistent with literature describing the current OHC mechanistic understanding. In their pioneering paper, Paolucci et al. reported that a Cu-oxo dimer is necessary to facilitate the low-temperature SCR OHC [9]. Subsequent publications from various other groups allude to the same
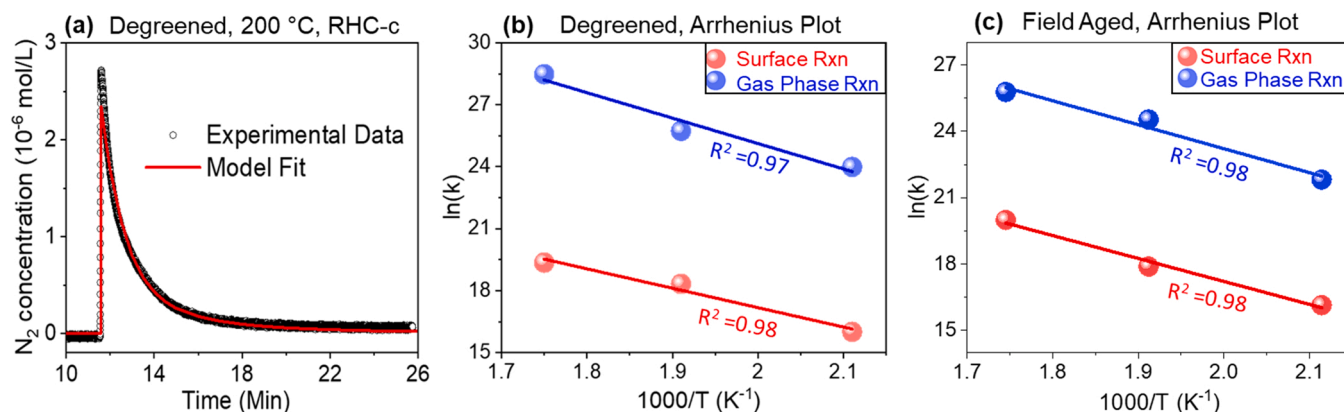
**Fig. 11.** (a) Experimental $N_2$ formation transient at 200 °C and 1/8 L for the RHC-c step and corresponding model fit. Rate constants obtained from these fits are plotted against 1/T for the (b) DG catalyst and (c) FA catalyst.

**Table 3**
Activation energies for the surface and gas-phase RHC reactions and OHC (via $O_2$ only) of the DG and FA catalysts determined via transient-response methodology.

| Catalyst | Activation Energy: $E_{act}$ (kJ/mol) | | | |
|---|---|---|---|---|
| | RHC Surface Reaction | RHC Gas-Phase Reaction | OHC, Cu oxidation by $O_2$ | SCR |
| Degreened | 78 | 102 | 34 | 68 |
| Field Aged | 85 | 95 | 55 | 58 |

idea that simultaneous involvement of two Cu ions is required for OHC [8,47], and the second-order dependence highlighted in Fig. 12(b) confirms that two Cu ions are required for OHC.

The rate constants for the DG and FA catalysts, obtained from second-order fits of Cu oxidation kinetics in the 175–275 °C temperature range, are plotted against 1/T in Fig. 12(c). Both the DG and FA catalysts have linear ln(k)-vs-1/T plots, which were used to extract the associated OHC activation energies. Table 3 shows that the DG-catalyst's OHC activation energy is 34 kJ/mol, which is similar to that reported by Paolucci et al. and Chen et al. based on DFT calculations [9,48,49]. The activation energy of the FA catalyst is 55 kJ/mol, or 60% greater than that of the DG catalyst. Thus, field aging of the Cu-SSZ-13 catalyst significantly increases the energy requirement for the SCR OHC and contributes to the degraded performance of the FA catalyst shown in Fig. 8. Furthermore, based on Table 3 and consistent with the TRCR-protocol results of Figs. 9c and 10(b), field ageing selectively degrades the OHC.

### 3.10. Field aging impact on global-SCR kinetics

The global performance measurements, characterization, and half-cycle kinetic analysis are consistent with the impact of field aging on the global-SCR kinetics. Section 3.7 and Fig. 8 showed how the global-SCR performance of Cu-SSZ-13 deteriorates significantly following field aging. Material characterization via ICP and $SO_2$ TPD elucidated how a fraction of the active Cu sites is deactivated by S- and P-related poisons originating from fuel and lubricants, which leads to a decrease in SCR performance. Although field aging changes the $Z_1CuOH$ and $Z_2Cu$ speciation, as shown by $H_2$-TPR, both sites can experience varying degrees of sulfur poisoning [15]. Field aging also leads to loss of ion-exchanged Cu via dealumination, as seen from NMR data. Sections 3.8 and 3.9 demonstrate how the transient-response methodology can be used to determine half-cycle kinetic parameters and quantify the impact of field ageing on RHC and OHC, and how these insights are consistent with aging impact directly apparent from the experimental TRCR-protocol results. Field aging degrades Cu-SSZ-13 SCR performance via two related pathways: (1) a decrease in the number of active reducible-Cu sites, and (2) kinetic impact on the SCR redox half cycles. Field aging has a minimal impact on RHC, but substantially degrades OHC. Field aging of Cu-SSZ-13 includes HTA and sulfur-aging components, which occur throughout the catalyst's on-road lifetime. Exposure to sulfur causes formation of various sulfur-based species, such as bisulfite, bisulfate and sulfate, adsorbed onto the active Cu sites and (extra-) framework aluminum. Such sulfur species can either deactivate the Cu sites completely, or hinder the formation of Cu-dimers, such as $[(NH_3)_2Cu(II)-O_2-Cu(II)(NH_3)_2]$ proposed by Paolucci et al., that are
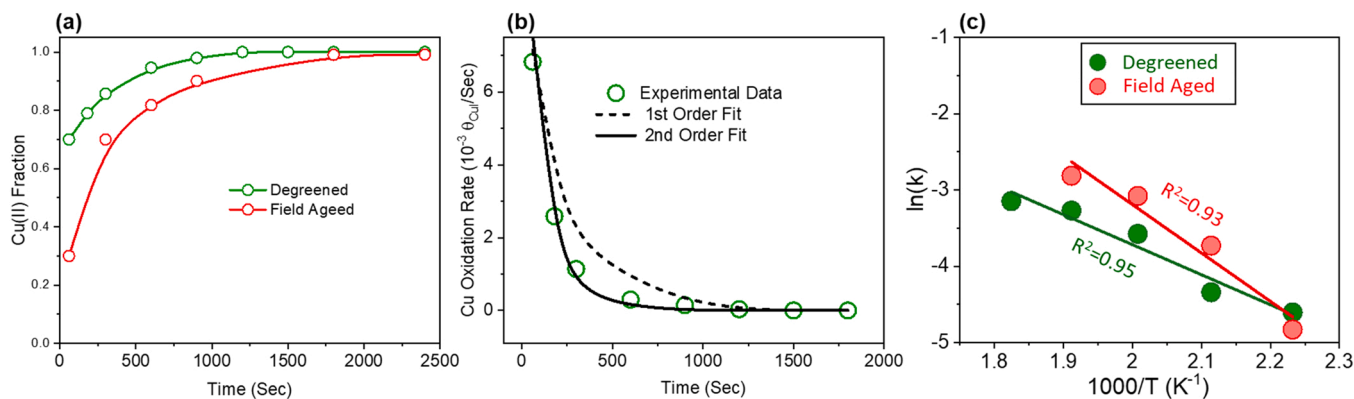


**Fig. 12.** (a) Fraction of oxidized Cu at 200 °C on the DG and FA catalysts as a function of oxidation time, at 3/16 L and 1/4 L catalyst locations, respectively, (b) Cu oxidation rate of the DG catalyst at 200 °C and fits using the OHC model (Eq. 19) with first-order and second-order kinetics, (c) Arrhenius plots of second-order rate constants for the DG and FA catalysts in 175–275 °C range.
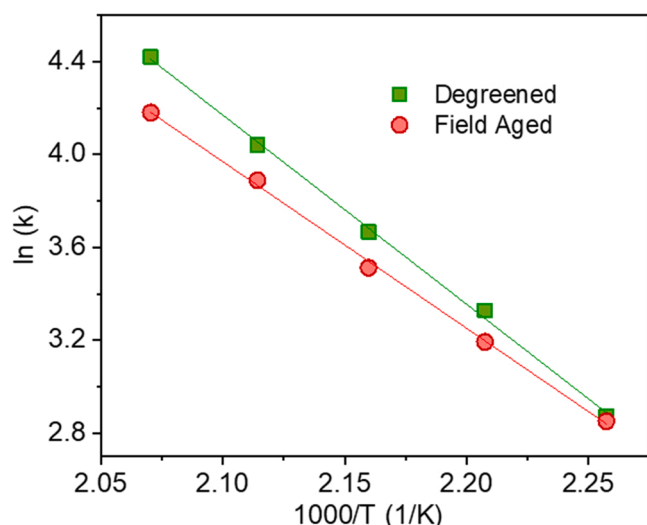
**Fig. 13.** Arrhenius plot of the SCR reaction at 1/16 L location within the DG and FA catalysts and five temperatures, 170, 180, 190, 200, and 210 °C. Reaction conditions: 40,000/h integral SV (640,000/h SV at 1/16 L), 200 ppm NO, 200 ppm NH$_3$, 5% O$_2$, 5% H$_2$O and Argon balance.

TPD, SO$_2$ TPD, ICP and solid-state NMR experiments.

- H$_2$-TPR and NH$_3$-adsorption DRIFTS show that the FA catalyst has higher Z$_1$CuOH fraction than the DG catalyst because a fraction of the Z$_2$Cu is converted to Z$_1$CuOH during field aging. Such changes in Cu speciation alters the average NH$_3$ coordination of the Cu sites, since the Z$_2$Cu can adsorb more NH$_3$ than Z$_1$CuOH. The ICP results show that the FA catalyst contains sulfur and phosphorus impurities while NMR reveals existence of dealumination of framework aluminum; these lead to a decrease in reducible-Cu site density in the FA catalyst. The loss of total reducible Cu, changes in Cu speciation and NH$_3$ coordination deteriorates the global SCR performance of Cu-SSZ-13.
- Loss of reducible Cu deteriorates the SCR activity of the FA catalyst. However, SCR turnover rates were lower on the FA catalyst compared to the DG catalyst; this indicated that loss of active Cu sites was not the sole reason for SCR performance degradation in the FA catalyst, and that the SCR redox half-cycle (RHC and OHC) kinetics were also impacted by field aging.
- A transient-response methodology composed of experimental TRCR-protocol measurements, kinetic modeling, and data fitting provide a framework for quantifying RHC and OHC kinetics and how they are impacted by aging. The experimental portion provides for assessing relative impacts of aging on the individual half cycles, while the full methodology provides for quantifying half-cycle activation energies.
- Conversion inflections of the SCR steps in the TRCR protocol illustrated that field aging impacts RHC kinetics minimally but significantly impacts the OHC kinetics. Additionally, the Cu(II) fraction at steady state SCR was found to be lower for the FA catalyst, demonstrating that field aging selectively slows OHC more than RHC.
- An RHC kinetic model was created based on two reduction pathways: a surface route involving reaction between NH$_3$-solvated Cu and NO, and a gas-phase route accounting for reactions between gas-phase NH$_3$ and NO. A simple kinetic model describing O$_2$-only OHC was also created in this study.
- Using the RHC and OHC kinetic models to fit the transient TRCR-protocol data allowed activation energies of the surface and gas-phase RHC pathways and OHC to be determined in the NH$_3$-solvation or low-temperature range (<300 °C). These showed similar low-temperature RHC activation energies (both surface and gas-phase pathways) for the DG and FA catalysts, but 60% higher OHC activation energy for the FA catalyst compared to the DG state. These results are consistent with the experimental evidence provided by SCR CI and Cu(II) fraction at SS SCR, and indicate that field aging impacts OHC more than RHC.
- The activation energy for low-temperature Standard SCR under differential conditions was determined. The SCR activation energy for the DG catalyst was between the RHC and OHC activation energies, while that for the FA catalyst was closer to the OHC activation energy, indicating that SCR on the FA catalyst is relatively more OHC-limited. Such knowledge of how field ageing selectively impacts the SCR reaction half cycles is relevant to developing catalyst formulations for improved performance; e.g., for the catalyst studied here, improved OHC aging durability would improve SCR performance over the useful life.

required for the OHC [9]. This may result in a greater activation-energy requirement for Cu-dimer formation and therefore OHC in general. This section focuses on rationalizing the field-aging impacts on the individual RHC and OHC half cycles in the context of the full SCR Cu-redox cycle.

The impact of real-world field ageing on the SCR activation energy is controlled by and can be more deeply understand by how field ageing impacts the RHC and OHC activation energies. To demonstrate and investigate this, we measured the SCR activation energy for the DG and FA catalysts and compared those to that of the individual half cycles. The SCR-reaction activation energy was measured in the temperature range 170–210 °C from kinetic data collected at 1/16 L location (high space velocity of 640,000/h) that fall within the kinetically limited region (<15% NO conversion). First-order reaction with respect to NO, Rate$_{SCR}$ = k$_{SCR}$. C$_{NO}$ was assumed [14,15], and the Arrhenius rate constants 'k' at these five temperatures were calculated and co-plotted in Fig. 13 to determine SCR activation energies for the two catalyst samples; the resulting activation energies are 68 kJ/mol and 58 kJ/mol for the DG and FA catalysts, respectively (Table 3). Activation energies in the range 60–85 kJ/mol have been reported for low-temperature SCR on DG and HTA catalysts by various literature studies [5,14,16,50]. The measured DG SCR activation energy (68 kJ/mol, Table 3) is between that of the two half cycles and not strongly dominated by either. The literature also reports that the SCR activation energies could decrease to ~50 kJ/mol on sulfated Cu-SSZ-13 catalysts [14,15], which is similar to the value we measure for the FA catalyst (58 kJ/mol, Table 3). Such degraded FA-catalysts SCR performance could result from OHC becoming the rate-limiting step. Indeed, the calculated OHC and SCR activation energies of the FA catalyst (Table 3) are similar and suggest relatively more OHC-limited SCR compared to the DG state. This demonstrates a consistency between individual-half-cycle and SCR aging studies, and how studying RHC and OHC aging provides a deeper understanding of the origins of aging-related SCR performance degradation.

## 4. Conclusion

In this study, the impact of real-world field aging on the Cu-redox half cycles of a commercial Cu-SSZ-13 catalyst was investigated using a transient-response Cu-redox (TRCR) methodology that consisted of transient response experiments and kinetic modeling. Changes in catalyst chemical properties caused by field aging were also examined via various characterization techniques including H$_2$-TPR, DRIFTS, NH$_3$

To our knowledge, this is the first full research article focused on kinetic impact of field aging on the SCR redox half cycles of a Cu-SSZ-13 catalyst. The SCR CI, RHC and OHC transients are reported for the first time along with associated kinetic models to calculate the half cycle activation energies. Such knowledge of how real-world field aging impacts specific half cycles and kinetic parameters is relevant to improving SCR catalyst design, formulation, control, and in-use diagnosis methods. Ongoing work investigates the SCR redox transients on HTA and lab-sulfated samples in order to break down the component contribution of HTA and sulfur exposure to field aging and will be published in the

near future.

## CRediT authorship contribution statement

**Dhruba J. Deka:** Conceptualization, Methodology, Validation, Formal analysis, Investigation, Writing – original draft, Writing – review & editing, Visualization. **Rohil Daya:** Methodology, Resources, Writing – review & editing. **Austin Ladshaw:** Methodology, Software, Writing – review & editing. **Dylan Trandal:** Methodology, Resources, Writing – review & editing. **Saurabh Y. Joshi:** Methodology, Resources, Writing – review & editing, Supervision, Project administration, Funding acquisition. **William P. Partridge:** Conceptualization, Methodology, Validation, Formal analysis, Investigation, Resources, Writing – original draft, Writing – review & editing, Visualization, Supervision, Project administration, Funding acquisition.

## Declaration of Competing Interest

The authors declare that they have no known competing financial interests or personal relationships that could have appeared to influence the work reported in this paper.

## Acknowledgements

## Appendix A. Supporting information

Supplementary data associated with this article can be found in the online version at doi:10.1016/j.apcatb.2022.121233.

## References

[1] S. Brandenberger, O. Kröcher, A. Tissler, R. Althoff, The state of the art in selective catalytic reduction of NOx by ammonia using metal-exchanged zeolite catalysts, Catal. Rev. 50 (2008) 492–531.

[2] J.H. Kwak, R.G. Tonkyn, D.H. Kim, J. Szanyi, C.H.F. Peden, Excellent activity and selectivity of Cu-SSZ-13 in the selective catalytic reduction of NOx with NH3, J. Catal. 275 (2010) 187–190.

[3] J. Luo, H. An, K. Kamasamudram, N. Currier, A. Yezerets, T. Watkins, L. Allard, Impact of accelerated hydrothermal aging on structure and performance of Cu-SSZ-13 SCR catalysts, SAE Int. J. Engines 8 (2015) 1181–1186.

[4] F. Gao, E.D. Walter, E.M. Karp, J. Luo, R.G. Tonkyn, J.H. Kwak, J. Szanyi, C.H. F. Peden, Structure–activity relationships in NH3-SCR over Cu-SSZ-13 as probed by reaction kinetics and EPR studies, J. Catal. 300 (2013) 20–29.

[5] F. Gao, E.D. Walter, M. Kollar, Y. Wang, J. Szanyi, C.H.F. Peden, Understanding ammonia selective catalytic reduction kinetics over Cu/SSZ-13 from motion of the Cu ions, J. Catal. 319 (2014) 1–14.

[6] C. Paolucci, A.A. Verma, S.A. Bates, V.F. Kispersky, J.T. Miller, R. Gounder, W. N. Delgass, F.H. Ribeiro, W.F. Schneider, Isolation of the copper redox steps in the standard selective catalytic reduction on Cu-SSZ-13, Angew. Chem. Int. Ed. Engl. 53 (2014) 11828–11833.

[7] C. Paolucci, J. Di Iorio, F. Ribeiro, R. Gounder, W. Schneider, Catalysis science of NOx selective catalytic reduction with ammonia over Cu-SSZ-13 and Cu-SAPO-34, Adv. Catal. 59 (2016) 1–107.

[8] F. Gao, D. Mei, Y. Wang, J. Szanyi, C.H. Peden, Selective catalytic reduction over Cu/SSZ-13: linking homo- and heterogeneous catalysis, J. Am. Chem. Soc. 139 (2017) 4935–4942.

[9] C. Paolucci, I. Khurana, A.A. Parekh, S. Li, A.J. Shih, H. Li, J.R. Di Iorio, J. D. Albarracin-Caballero, A. Yezerets, J.T. Miller, Dynamic multinuclear sites formed by mobilized copper ions in NOx selective catalytic reduction, Science 357 (2017) 898–903.

[10] F. Gao, J. Szanyi, On the hydrothermal stability of Cu/SSZ-13 SCR catalysts, Appl. Catal. A: Gen. 560 (2018) 185–194.

[11] S.J. Schmieg, S.H. Oh, C.H. Kim, D.B. Brown, J.H. Lee, C.H. Peden, D.H. Kim, Thermal durability of Cu-CHA NH3-SCR catalysts for diesel NOx reduction, Catal. Today 184 (2012) 252–261.

[12] J. Luo, F. Gao, K. Kamasamudram, N. Currier, C.H.F. Peden, A. Yezerets, New insights into Cu/SSZ-13 SCR catalyst acidity. Part I: Nature of acidic sites probed by NH3 titration, J. Catal. 348 (2017) 291–299.

[13] J. Luo, D. Wang, A. Kumar, J. Li, K. Kamasamudram, N. Currier, A. Yezerets, Identification of two types of Cu sites in Cu/SSZ-13 and their unique responses to hydrothermal aging and sulfur poisoning, Catal. Today 267 (2016) 3–9.

[14] Y. Xi, C. Su, N.A. Ottinger, Z.G. Liu, Effects of hydrothermal aging on the sulfur poisoning of a Cu-SSZ-13 SCR catalyst, Appl. Catal. B: Environ. 284 (2021), 119710.

[15] Y. Jangjou, Q. Do, Y. Gu, L.-G. Lim, H. Sun, D. Wang, A. Kumar, J. Li, L.C. Grabow, W.S. Epling, Nature of Cu active centers in Cu-SSZ-13 and their responses to SO2 exposure, ACS Catal. 8 (2018) 1325–1337.

[16] A.J. Shih, I. Khurana, H. Li, J. González, A. Kumar, C. Paolucci, T.M. Lardinois, C. B. Jones, J.D. Albarracin Caballero, K. Kamasamudram, A. Yezerets, W.N. Delgass, J.T. Miller, A.L. Villa, W.F. Schneider, R. Gounder, F.H. Ribeiro, Spectroscopic and kinetic responses of Cu-SSZ-13 to SO2 exposure and implications for NOx selective catalytic reduction, Appl. Catal. A: Gen. 574 (2019) 122–131.

[17] K. Wijayanti, S. Andonova, A. Kumar, J. Li, K. Kamasamudram, N.W. Currier, A. Yezerets, L. Olsson, Impact of sulfur oxide on NH3-SCR over Cu-SAPO-34, Appl. Catal. B: Environ. 166 (2015) 568–579.

[18] C.A.R. Board, Proposed Heavy-Duty Engine and Vehicle Omnibus Regulation, 2020.

[19] D.J. Deka, R. Daya, A. Ladshaw, S.Y. Joshi, W.P. Partridge, A Transient-Response Methodology based on Experiments and Modeling for Cu-Redox Half-Cycle Kinetic Analysis on a Cu-SSZ-13 SCR Catalyst, Chemical Engineering Journal 435 (2022) 134219.

[20] J.-S. Choi, W.P. Partridge, J.A. Pihl, M.-Y. Kim, P. Kočí, C.S. Daw, Spatiotemporal distribution of NOx storage and impact on NH3 and N2O selectivities during lean/ rich cycling of a Ba-based lean NOx trap catalyst, Catal. Today 184 (2012) 20–26.

[21] W.P. Partridge, S.Y. Joshi, J.A. Pihl, N.W. Currier, New operando method for quantifying the relative half-cycle rates of the NO SCR redox cycle over Cu-exchanged zeolites, Appl. Catal. B: Environ. 236 (2018) 195–204.

[22] W.P. Partridge Jr., J.-S. Choi, Understanding the performance of automotive catalysts via spatial resolution of reactions inside honeycomb monoliths, Adv. Chem. Eng. Elsevier (2017) 1–81.

[23] K. Morgan, J. Touitou, J.-S. Choi, C. Coney, C. Hardacre, J.A. Pihl, C.E. Stere, M.-Y. Kim, C. Stewart, A. Goguet, W.P. Partridge, Evolution and enabling capabilities of spatially resolved techniques for the characterization of heterogeneously catalyzed reactions, ACS Catal. 6 (2016) 1356–1381.

[24] M. Hettel, C. Diehm, B. Torkashvand, O. Deutschmann, Critical evaluation of in situ probe techniques for catalytic honeycomb monoliths, Catal. Today 216 (2013) 2–10.

[25] W. Hu, T. Selleri, F. Gramigni, E. Fenes, K.R. Rout, S. Liu, I. Nova, X. Chen, E. Gao, Tronconi, On the redox mechanism of low-temperature NH3 -SCR over Cu-CHA: a combined experimental and theoretical study of the reduction half cycle, Angew. Chem. Int. Ed. Engl. 60 (2021) 7197–7204.

[26] N. Usberti, F. Gramigni, N.D. Nasello, U. Iacobone, T. Selleri, W. Hu, S. Liu, X. Gao, I. Nova, E. Tronconi, An experimental and modelling study of the reactivity of adsorbed NH3 in the low temperature NH3-SCR reduction half-cycle over a Cu-CHA catalyst, Appl. Catal. B: Environ. 279 (2020).

[27] F. Gramigni, N.D. Nasello, N. Usberti, U. Iacobone, T. Selleri, W. Hu, S. Liu, X. Gao, I. Nova, E. Tronconi, Transient kinetic analysis of low-temperature NH3-SCR over Cu-CHA catalysts reveals a quadratic dependence of Cu reduction rates on cuII, ACS Catal. 11 (2021) 4821–4831.

[28] J. Song, Y. Wang, E.D. Walter, N.M. Washton, D. Mei, L. Kovarik, M.H. Engelhard, S. Prodinger, Y. Wang, C.H. Peden, Toward rational design of Cu/SSZ-13 selective catalytic reduction catalysts: implications from atomic-level understanding of hydrothermal stability, ACS Catal. 7 (2017) 8214–8227.

[29] F. Gao, E.D. Walter, N.M. Washton, J. Szanyi, C.H. Peden, Synthesis and evaluation of Cu/SAPO-34 catalysts for NH3-SCR 2: Solid-state ion exchange and one-pot synthesis, Appl. Catal. B: Environ. 162 (2015) 501–514.

[30] R. Daya, S.Y. Joshi, J. Luo, R.K. Dadi, N.W. Currier, A. Yezerets, On kinetic modeling of change in active sites upon hydrothermal aging of Cu-SSZ-13, Appl. Catal. B: Environ. 263 (2020).

[31] R. Daya, D. Trandal, R.K. Dadi, H. Li, S.Y. Joshi, J. Luo, A. Kumar, A. Yezerets, Kinetics and thermodynamics of ammonia solvation on Z2Cu, ZCuOH and ZCu sites in Cu-SSZ-13 – implications for hydrothermal aging, Appl. Catal. B: Environ. 297 (2021).

[32] V. Mesilov, S. Dahlin, S.L. Bergman, S. Xi, J. Han, L. Olsson, L.J. Pettersson, S. L. Bernasek, Regeneration of sulfur-poisoned Cu-SSZ-13 catalysts: copper speciation and catalytic performance evaluation, Appl. Catal. B: Environ. 299 (2021), 120626.

[33] K. Xie, J. Woo, D. Bernin, A. Kumar, K. Kamasamudram, L. Olsson, Insights into hydrothermal aging of phosphorus-poisoned Cu-SSZ-13 for NH3-SCR, Appl. Catal. B: Environ. 241 (2019) 205–216.

[34] O. Saur, M. Bensitel, A.M. Saad, J. Lavalley, C.P. Tripp, B. Morrow, The structure and stability of sulfated alumina and titania, J. Catal. 99 (1986) 104–110.

[35] J. Pérez-Pariente, J. Sanz, V. Fornés, A. Corma, 29Si and 27Al MAS NMR study of zeolite β with different Si/Al Ratios, J. Catal. 124 (1990) 217–223.

[36] C.J. Jacobsen, C. Madsen, T.V. Janssens, H.J. Jakobsen, J. Skibsted, Zeolites by confined space synthesis–characterization of the acid sites in nanosized ZSM-5 by

ammonia desorption and 27Al/29Si-MAS NMR spectroscopy, Microporous Mesoporous Mater. 39 (2000) 393–401.

[37] S. Greiser, G.J. Gluth, P. Sturm, C. Jäger, 29 Si {27 Al}, 27 Al {29 Si} and 27 Al {1H} double-resonance NMR spectroscopy study of cementitious sodium aluminosilicate gels (geopolymers) and gel–zeolite composites, RSC Adv. 8 (2018) 40164–40171.

[38] M. Haouas, F. Taulelle, C. Martineau, Recent advances in application of 27Al NMR spectroscopy to materials science, Prog. Nucl. Magn. Reson. Spectrosc. 94 (2016) 11–36.

[39] Z. Zhao, S. Xu, M.Y. Hu, X. Bao, C.H. Peden, J. Hu, Investigation of aluminum site changes of dehydrated zeolite H-beta during a rehydration process by high-field solid-state NMR, J. Phys. Chem. C 119 (2015) 1410–1417.

[40] R. Zhang, Z. Wang, Y. Meng, S. Jiao, J. Jia, Y. Min, C. Liu, Quantitative insight into aluminum structures in CaO–Al2O3–SiO2 system via Raman and 27Al MAS NMR spectroscopies, J. Non-Cryst. Solids 573 (2021), 121116.

[41] K. Kamasamudram, N.W. Currier, X. Chen, A. Yezerets, Overview of the practically important behaviors of zeolite-based urea-SCR catalysts, using compact experimental protocol, Catal. Today 151 (2010) 212–222.

[42] A. Ladshaw, J. Pihl, Measurement and Modeling of the effects of exhaust composition and hydrothermal aging on the ammonia storage capacity of a commercial Cu-SSZ-13 catalyst, Appl. Catal. B: Environ. (2021), 120898.

[43] M. Moreno-Gonzalez, B. Hueso, M. Boronat, T. Blasco, A. Corma, Ammonia-containing species formed in Cu-chabazite as per in situ EPR, solid-state NMR, and DFT calculations, J. Phys. Chem. Lett. 6 (2015) 1011–1017.

[44] C. Paolucci, A.A. Parekh, I. Khurana, J.R. Di Iorio, H. Li, J.D. Albarracin Caballero, A.J. Shih, T. Anggara, W.N. Delgass, J.T. Miller, F.H. Ribeiro, R. Gounder, W. F. Schneider, Catalysis in a cage: condition-dependent speciation and dynamics of exchanged Cu cations in SSZ-13 zeolites, J. Am. Chem. Soc. 138 (2016) 6028–6048.

[45] R. Daya, C.J. Keturakis, D. Trandal, A. Kumar, S.Y. Joshi, A. Yezerets, Alternate pathway for standard SCR on Cu-zeolites with gas-phase ammonia, React. Chem. Eng. 6 (2021) 1042–1052.

[46] S.H. Krishna, C.B. Jones, R. Gounder, Temperature dependence of Cu (I) oxidation and Cu (II) reduction kinetics in the selective catalytic reduction of NOx with NH3 on Cu-chabazite zeolites, J. Catal. (2021).

[47] A. Oda, H. Shionoya, Y. Hotta, T. Takewaki, K. Sawabe, A. Satsuma, Spectroscopic evidence of efficient generation of dicopper intermediate in selective catalytic reduction of NO over Cu-ion-exchanged zeolites, ACS Catalysis 10 (2020) 12333–12339.

[48] L. Chen, H. Falsig, T.V. Janssens, H. Grönbeck, Activation of oxygen on (NH3CuNH3)+ in NH3-SCR over Cu-CHA, J. Catal. 358 (2018) 179–186.

[49] L. Chen, T.V. Janssens, P.N. Vennestrøm, J. Jansson, M. Skoglundh, H. Gronbeck, A complete multisite reaction mechanism for low-temperature NH3-SCR over Cu-CHA, ACS Catal. 10 (2020) 5646–5656.

[50] Y. Feng, X. Wang, T.V. Janssens, P.N. Vennestrøm, J. Jansson, M. Skoglundh, H. Grönbeck, First-principles microkinetic model for low-temperature nh3-assisted selective catalytic reduction of NO over Cu-CHA, ACS Catal. 11 (2021) 14395–14407.